Journal of *Marine Science and Engineering*

MDPI

Article

Comparative Analysis of Scour in Riprap-Protected Monopiles and Hybrid Foundations

João Chambel [1,2,*], Tiago Fazeres-Ferradosa [1,2], Mario Welzel [3], Francisco Taveira-Pinto [1,2] and Pedro Lomónaco [4]

[1] Department of Civil Engineering and Georesources, Faculty of Engineering, University of Porto (FEUP), Rua Dr. Roberto Frias s/n, 4200-465 Porto, Portugal; tferradosa@fe.up.pt (T.F.-F.); fpinto@fe.up.pt (F.T.-P.)
[2] Marine Energy and Hydraulic Structures Research Group, Interdisciplinary Center of Marine and Environmental Research (CIIMAR-LA), University of Porto, Port of Leixões Cruise Terminal, Av. General Norton de Matos s/n, 4450-208 Matosinhos, Portugal
[3] Ludwig-Franzius-Institute for Hydraulic, Estuarine, and Coastal Engineering, Leibniz University Hannover, 30167 Hannover, Germany; welzel@lufi.uni-hannover.de
[4] O.H. Hinsdale Wave Research Laboratory, College of Engineering, Oregon State University (OSU), Corvallis, OR 97331, USA; pedro.lomonaco@oregonstate.edu
* Correspondence: up201304674@fe.up.pt

Abstract

As the demand for new sustainable solutions for harvesting energy increases, the offshore energy sector focuses on optimising well-established state-of-the-art solutions while striving for new innovative approaches. Hybrid foundation designs have introduced new challenges and raised questions regarding scour and effective countermeasures. To further improve the knowledge regarding scour prediction, this paper presents and analyses the results from an experimental study behaviour of a riprap protection system for a monopile that determines and characterises scour on a flexible arrangement of overlapping sub-areas. The study was complemented by a novel series of tests using a hybrid foundation, where an oscillating surge wave energy converter (OSWEC) type was coupled to the monopile. Despite being submitted to similar hydrodynamic conditions, distinct differences in the scour rate and damage number (S_{3D}) were observed for both models. Although the OSWEC type contributed to local wave height attenuation (up to a 30% reduction on the leeward side of the hybrid monopile), its oscillatory motion severely aggravated scour, with measured damage rates two to three times higher than those observed in isolated monopiles. These results raise relevant questions about the applicability of existing design formulas for scour protection and underscore the necessity for revised criteria tailored to hybrid offshore foundations.

Keywords: offshore renewable energy; scour protection; monopiles; wave energy converter; hybrid foundations

check for updates

Academic Editor: Pietro Scandura

Received: 18 July 2025
Revised: 11 August 2025
Accepted: 24 August 2025
Published: 27 August 2025

Citation: Chambel, J.; Fazeres-Ferradosa, T.; Welzel, M.; Taveira-Pinto, F.; Lomónaco, P. Comparative Analysis of Scour in Riprap-Protected Monopiles and Hybrid Foundations. *J. Mar. Sci. Eng.* **2025**, *13*, 1639. https://doi.org/10.3390/jmse13091639

Copyright: © 2025 by the authors. Licensee MDPI, Basel, Switzerland. This article is an open access article distributed under the terms and conditions of the Creative Commons Attribution (CC BY) license (https://creativecommons.org/licenses/by/4.0/).

1. Introduction

1.1. Background

Offshore wind energy research has grown rapidly, becoming a key component of a global renewable energy strategies. The structural integrity and long-term stability of offshore wind turbine (OWT) foundations, predominantly using monopiles [1], are critical for ensuring economic feasibility and safety. A primary concern regarding the stability of the foundation, which entails around one-third of the overall investment [2,3], is scour, a

common cause of interference in bearing capacity, the ultimate, and service limit states [4,5]. Various countermeasures, such as riprap protections, represent an essential part of that investment [6] and are commonly installed at the base of these structures to mitigate scour-related challenges. Implementing these countermeasures follows established empirical guidelines [7]. Existing design formulas and approaches are commonly monopile-related, creating a lack of a general understanding of scour development at more complex structures, such as jackets, gravity-based foundations (GBF), tripods, or even hybrid foundations [8]. The concept of hybrid energy solutions, i.e., the co-location of wave energy converters (WEC) with offshore wind foundations, has developed increasing interest from the scientific community and the private sector. Enhancing energy yield and optimising spatial utilisation of marine areas could help lower the levelised energy cost (LCoE). It remains unclear to what extent sediment mobilization and altered flow patterns caused by hybrid monopile structures impact the marine environment both near the foundation and in the far field. While WECs are designed to extract energy from waves, their presence can modify in-depth hydrodynamics, wave propagation, current patterns, turbulence levels, and scour mechanisms (downflow, horseshoe, and/or lee–wake vortices) around the foundation. Understanding the impact of these changes on the performance and stability of existing scour protections is crucial for a safe and efficient deployment of hybrid offshore energy systems.

Several authors have studied the effectiveness and behaviour of riprap protections, inspired by rubble-mound breakwaters. This type of countermeasure is widely used due to its low cost and material availability, although transport and installation costs may vary with the location, armour layer thickness, and required stone size [9,10], among other aspects.

1.2. Scour Protections: Design

The threshold of motion concept by [11], was one of the first studies providing insights into scour and scour protection design. This type of protection was later classified as static by [7,12] since the movement of the elements of the armour layer is not allowed. Hence, the median stone size (D_{50}) should be determined so the shear stress induced by the offshore conditions is smaller than the critical shear stress (τ_{cr}) of the rock material—Equation (1), where ρ_s is the mass density of the material, ρ_w is the water mass density, θ_{cr} is the critical Shields parameter, which for non-cohesive soils is given by Equation (2), and is dependent on the dimensionless grain size (D*), Equation (3), where ν is the kinematic viscosity of water. For $D^* > 100$ on non-cohesive soils, θ_{cr} has the asymptotic value of 0.056.

$$\tau_{cr} = \theta_{cr} g(\rho_s - \rho_w) D_{50} \quad (1)$$

$$\theta_{cr} = \frac{0.3}{1 + 1.2D^*} + 0.055(1 - exp[-0.02D^*]) \quad (2)$$

$$D^* = D_{50}\left(\frac{g(s|-|1)}{v_2}\right)^{1/3} \quad (3)$$

An amplification factor (α) for monopiles should reflect the foundation's effect on enhancing the flow conditions and the associated shear stress [13,14]. An alternative way to obtain the maximum wave-and-current-induced shear stress for wide graded protections was provided by [15], but the formula uses the $D_{67.5}$ value for a $\theta_{cr} = 0.035$, instead of D_{50}.

The conservative approach of static design led to expensive solutions, given the larger stone size applied, but it is the most common type of countermeasure used in commercial offshore wind projects [9,10]. An optimisation was introduced by [12] in the OPTI-PILE project, the concept of dynamic protection, which allowed for the controlled movement of the armour layer elements, thus reducing both the size, thickness, and volume of the material needed [2]. This new approach, [12], proposed a stability parameter (stab),

Equation (4), where θ_{max} is the maximum dimensionless wave–current-induced shear stress. The threshold of motion ceases to be the design criterion, and [12] defines failure when the filter layer is exposed to an area equivalent to $4D_{n50}^2$—an area equivalent to a square of two-by-two stones of D_{n50}.

$$stab = \theta_{max}/\theta_{cr} \quad (4)$$

Nonetheless, the stab parameter was still dependent on the amplification factor, whose values differ from author to author and cannot be extrapolated to more complex structures [8,9]. Therefore, the three-dimensional damage number (S_{3D}) for scour protection was introduced by [7,16], based on the concept of the two-dimensional number [17]. By performing an extensive physical model study, it was noted that the stab parameter failed to predict some of the motion caused under different hydrodynamic conditions. The advantage of the proposed S_{3D}, Equation (5), was that it is not dependent on the critical shear stress or the amplification factor, leaving behind some of the limitations of the considerations presented by [11,12,15], allowing a classification of the protection into three different levels of damage: static ($S_{3D} < 0.25$), dynamic ($0.25 < S_{3D} < 1.00$), and failure ($S_{3D} \geq 1.00$):

$$\frac{S_{3D}}{N^{b0}} = a_0 \frac{U_m^3 T_{m-1,0}^2}{\sqrt{gd}(s-1)^{3/2} D_{n50}^2} + a_1 \left(a_2 + a_3 \frac{(U_c/w_s)^2 (U_c + a_4 U_m)^2 \sqrt{d}}{g D_{n50}^{3/2}} \right) \quad (5)$$

where N is the number of waves, g is the gravitational acceleration, d is the water depth, U_m is the orbital velocity, $T_{m-1,0}$ is the energy wave period, s is the ratio between ρ_s and ρ_w, U_c is the depth-average velocity, w_s is the settling velocity, a_0, a_2, a_3 and b_0 are regression coefficients equal to 0.00076, −0.022, 0.0079, and 0.243, respectively, and a_1 and a_4 are coefficients for hydrodynamic conditions defined in [7,16].

Although the design concept of dynamic stability enables the optimisation of scour protections, testing conditions of the formula were extended by [18–20], concluding that:

- The design equation does not consider the thickness (t_s) and pile diameter (D_p) variables.
- The limits established for stability showed that some overlapping situations arose; thus, the failure condition could occur for values above the limit of 1.00.
- Like in the static protections, the equation was obtained using only monopile foundations and a short variety of water depths and layer thicknesses.
- The failure criterion used by [7] was the same as in [12]. So, for the reference sub-area of $4D_{n50}^2$, the maximum dynamic behaviour limit of $S_{3D} = 1.0$ has the physical meaning of the scour protection decreasing in thickness by a distance equal to D_{n50}. For scour protections with thicknesses over nD_{n50} ($n > 1$), $S_{3D} = 1.0$ may not be truly representative of failure.
- To quantify the S_{3D} values, the scour protection was divided into fixed sub-areas with an equal area to the monopile cross-section, thus neglecting the damage occurring in the intersection of the sub-areas, the effect of damage in adjacent sub-areas, and not considering the cumulative impact.

An alternative methodology [21] discusses a different way to analyse the damage by creating a mesh of overlapping circles placed in concentric rings, centred at the foundation with an adaptable overlapping distance, angle, and resolution, offering a more detailed assessment of the extent and severity of scour. The concept prevents an excessive lowering of damage due to the averaging of the scour depth over larger sub-areas, reduces deceptive damage interpretations, can be adapted to more complex structures, and enables a much larger population of S_{3D} values quantified over the scour protection's area, thus allowing for the statistical analysis of damage, describing failure with additional parameters (standard deviation, 95th percentile, etc.) rather than only using the maximum damage number. However, this methodology still lacks a detailed definition of the limits to classify

protections as dynamically or statically stable or failures. Hence, the literature shows a need for more physical modelling tests, such as the ones presented here, to address this gap.

The radius of the sub-area (R_{circle}) is given by two parameters, D_{n50} and a multiplication factor (p), Equation (7), which is chosen so that the area of the circle reflects a certain area (A_{sub}), such as, for example, the failure criterion [12]. A percentage of the radius defines the overlapping distance. However, according to [21], the overlapping distance has a reduced influence. No considerable gains were obtained for overlapping distances different from 50%. The S_{3D} is calculated by:

$$S_{3Dsub,\,circle} = \frac{V_{circle}}{D_{n50} \cdot \pi R_{circle}^2} \quad (6)$$

$$p = 2\sqrt{\frac{n}{\pi}}, \text{ for } A_{sub} = n \cdot D_{n50}^2 \quad (7)$$

The sub-area arrangement and the mesh characteristics were analysed by [21] by comparing results for different grid ratios. The measurements revealed a strong dependency of the damage number on the size of the sub-area (A_{sub}) and the $S_{3D,max}$, which increases significantly with increasing grid ratio, thus revealing that the grid ratio selection can completely impact the damage calculation and the scour protection behaviour assessment. This ratio, $\eta_{S3D,grid}$, is given by:

$$\eta_{S3D,grid} = \frac{D_{n50}^2}{A_{sub}} \quad (8)$$

An increase in the grid ratio for the same D_{n50}^2 results in a decrease in the sub-area. Varying the grid ratio also implies a variation in the number of elements. Therefore, a higher value of $\eta_{S3D,grid}$ indicates that the eroded volume pattern resembles more closely the digital terrain model (DTM). The conclusions derived from the variation of the $\eta_{S3D,grid}$ highlight the necessity for a uniform and justified selection of a criterion of failure and size of the sub-area. Hence, a statistical analysis was performed by [21] to determine if a specific $\eta_{S3D,grid}$ led to a convergence of the S_{3D} values, concluding that the variation between $\eta_{S3D,grid} = 0.25$ ($A_{sub} = 4D_{n50}^2$) and $\eta_{S3D,grid} = 0.5$ ($A_{sub} = 2D_{n50}^2$) seemed to be reasonably small, pointing to the failure criteria suggested by [12] to be a realistic limit to identify failure in scour protections. The research also concludes that, under this methodology, the acceptable damage number for dynamic scour protection needs to be defined, in opposition to the unit value formerly proposed. That implies larger datasets to analyse the influence of the armour layer thickness, the presence of a sand filter layer or geotextile, and the relation with parameters such as the Keulega–Carpenter (KC) and/or the Reynolds (Re) numbers.

1.3. Deformation and Mobility

More recently, ref. [22] performed an extensive database of 380 tests and claimed that the spatial deformation due to scour around a monopile is not unambiguous and that the classification and interpretation of scour protection's behaviour into classes is not straightforward. It requires the precise definition of what constitutes failure, which can often be "case-specific". It highlights that calculating the scour deformation depth could be more intuitive for design purposes. It points out that with only two parameters, it can quantitatively describe the deformation of a scour protection and presents a formula to predict it—Equation (9). These two parameters and their interpretable physical meaning are:

- MOB_{top} (relative mobility): measures the hydraulic loading at the top of the scour protection relative to the resistance of the armour layer material. In practical terms, this is the stab parameter presented by [12];
- KC_{tot} (Total Keulegan–Carpenter number): measures and evaluates the contribution of the wave-orbital and steady-current velocities relative to the structure. It measures

the wave stroke asymmetry and the bed shear stress amplification difference around the pile—Equation (10).

$$\frac{S}{D_p} = \left[1 + \frac{3.93}{1 + exp[-0.74KC_{tot} + 4.75]}\right] \cdot 0.07 \cdot MOB_{top}^{1.65} \quad (9)$$

$$KC_{tot} = \frac{(U_{m,top} + U_c) \cdot T_p}{D_p} \quad (10)$$

where S is the scour depth, $U_{m,top}$ is the wave-orbital velocity at the top of the scour protection, and T_p is the wave peak period.

Equation (9) only considers two parameters to prevent overfitting. Still, the impact of the material grading width, the storm duration, the ratio of water depth vs. pile diameter, the wave–current velocity ratio (U_{cw}), and many others was assessed. However, none seemed to depend on the deformation, such as MOB_{top} and KC_{tot}. Moreover, the results showed a weakly positive correlation between the two parameters, i.e., lower mobility numbers (relatively stable rocks) are associated with lower KC numbers (relatively large piles).

To measure deformations and to recognise the damage areas, a moving-disk filter algorithm was used [23], which separates scour deformation from sinking or sliding. However, the algorithm uses $A_{sub} = 20D_{50}^2$, an area equivalent to a circle with a diameter of $5D_{50}$. It is stated that the sub-area selected by [22] prevents recognition of spot deformation caused by the displacement of larger armour layer material, claiming that the failure criterion suggested by [12] does not eliminate spot deformation. By averaging a local spot deformation within a sub-area of $4D_{n50}^2$ over a circular area of $4D_{50}^2$, it only represents approximately a weight of 20% within the moving average area—the local spot deformation is not neglected but instead weighted differently. Based on the average damage pattern from the 380 tests, it is suggested that according to the respective values of the MOB_{top} and KC_{tot} the scour deformations occur in three distinct areas (upstream side of the pile, deposition area, and downstream side of the pile), which can be correlated to six different deformation pattern classes defined by [23]:

- Class 1: negligible deformation, small settlements, spot deformation, or slight local sinking ($1.5 \lesssim KC_{tot} \lesssim 4$ and $0.20 \lesssim MOB_{top} \lesssim 0.50$).
- Class 2: upstream deformation with negligible downstream deformation, associated with downflow pattern ($1.75 \lesssim KC_{tot} \lesssim 5$ and $0.20 \lesssim MOB_{top} \lesssim 0.85$).
- Class 3: evenly distributed upstream and downstream deformation. Increasing influence of lee–wake vortices ($2 \lesssim KC_{tot} \lesssim 5.5$ and $0.35 \lesssim MOB_{top} \lesssim 0.85$).
- Class 4: mainly downstream deformation. Higher prevalence of lee–wake vortices ($3.5 \lesssim KC_{tot} \lesssim 8$ and $0.40 \lesssim MOB_{top} \lesssim 1.10$).
- Class 5: deep upstream deformation combined with a single deep downstream deformation point. Can be difficult to distinguish from Class 4 but is highly related to the presence of a meaningful steady current ($2.5 \lesssim KC_{tot} \lesssim 9.5$ and $0.35 \lesssim MOB_{top} \lesssim 0.95$).
- Class 6: deformation mainly upstream with a single relatively shallow downstream deformation point. Associated with low current velocities or even only-wave conditions. Horseshoe vortices prevail over lee–wake vortices ($3.5 \lesssim KC_{tot} \lesssim 5$ and $0.6 \lesssim MOB_{top} \lesssim 0.8$);

By comparing tests with similar MOB_{top} and KC_{tot}, but with different contributions from waves and currents (only waves, wave-dominant conditions, and current-dominant conditions), it was observed that the predicted scour depth was in the same order of magnitude of the measured values—Equation (9) had a 0.85 correlation between the measured and the predicted S/D_p values [22]. Nonetheless, the author also underlines that the

formula can sometimes overestimate S/D_p for smaller values of KC_{tot}, and underestimate for larger values of KC_{tot}. Additionally, the deformation and scour pattern observed were significantly different, and sometimes some of the classes were difficult to distinguish, as evidenced by the overlapping range of values for both parameters. This observation was partially attributed to the asymmetry of the orbital wave motion when more intense current velocities exist. It emphasises that combining the hydrodynamic conditions is important to determine where the peak deformation will occur. In contrast, the values of the KC_{tot} and MOB_{top} parameters will predict the possible range of scour depth and damage. Finally, it suggests and emphasises the need to develop a design formula combining scour depth, area, and volume, with guidelines on the volume–area–depth relation and requirements for what constitutes a universal, clear, and unambiguous definition of scour protection failure.

1.4. Hybrid Structures

Although dynamic scour protection systems for monopiles have been the focus of the scientific community, significant knowledge gaps persist, particular due to limited data, and limited experimental studies about structures with complex geometries, hybrid structures, or other marine harvesting technologies in general [8]. The oscillatory or rotational motion of these devices induces additional soil-fluid-structure interactions, potentially causing significant alterations to wave orbital motion, current velocity fields and overall flow patterns. Standard scour protection behaviour and expected scour patterns may no longer apply. Therefore, design guidelines and equations could be misadjusted as they do not consider certain characteristics imposed by these devices. New design equations should consider not only structural and environmental parameters regarding the foundation and the offshore conditions, respectively, but also consider cyclical variations of pressure, disturbance/enhancement of flow patterns, wave reflection/attenuation, impact on soil properties, and vibration increments and/or modifications on the natural frequency of the structure. A review study on cases of scour on WECs and tidal–current energy converters (TECs) only, on WECs used as a protective measure in front of pipelines and monopiles, and even on WECs or TECs incorporated into breakwaters and monopiles, respectively, was performed by [8]. None of those studies used scour protections, and different results were reported: from no scour detection to reductions in the scour rates in the vicinity of structures to detrimental cases where scour rates were enhanced.

Due to the lack of consensus on reports and the absence of scientific studies using scour protections for hybrid offshore foundations, the present work provides a comparative experimental study that applies a riprap scour protection to both a monopile and a hybrid monopile foundation. The hybrid configuration was obtained by an in-house adaptation of a WEC [24–26] to the specific dimensions of the experimental setup. The riprap scour protection was designed based on the configuration and methodology used by [7]. However, instead of determining the varying median stone diameter (D_{n50}) for the intended hydrodynamic conditions, the study estimated the damage number and the scour depth across a range of wave and current combinations for the same scour protection configuration. The approach allowed for predicting the protection's behaviour regime (static, dynamic, or failure), thus enabling a comparison between the expected results and the experimentally measured outcomes. For the scour measurements, the overlapping methodology was used [21] to characterise scour damage in rubble mound scour protections and other marine structures, based on the statistical analysis of damage distribution in flexible meshes of overlapping circular sub-areas. Subsequently, a cautious and meticulous study of all relevant variables was conducted, drawing upon the insights from the literature. The aim was to encapsulate the existing knowledge and most recent research on offshore foundation scour protection, pointing out potential knowledge gaps and research synergies.

The findings reveal that despite the WEC-induced attenuation of the incident hydrodynamic conditions, its oscillatory motion induces complex flow patterns (including enhanced downflow, horseshoe vortices, and lee–wake vortices) that lead to irreversible damage to the riprap protection layer. Moreover, successfully applying the overlapping circles method to determine S_{3D} for scour damage assessment provides a precise damage quantification. However, the obtained damage values raise significant questions regarding the applicability and conservatism of existing design criteria and formulas proposed for monopiles [7,15], and in the context of hybrid foundation systems. This research contributes to a deeper understanding of the hydrodynamic interactions within hybrid offshore energy farms. It provides critical insights for designing and maintaining scour protection measures in such complex environments. These results emphasise the need for new criteria and guidelines for designing protective measures for a broader spectrum of offshore and marine technologies and structures.

2. Experimental Setup

2.1. Wave–Current Flume

The experimental work was carried out in the wave-and-current flume of the Hydraulics Laboratory of the Hydraulics, Water Resources, and Environmental Division (LH-SHRHA) in the Faculty of Engineering of the University of Porto—FEUP (Portugal). The infrastructure is 29 m long, 1 m wide, and 1 m deep, fed by a constant head reservoir. The sediment pit in the middle of the flume has a length of 3.4 m, a width of 1 m, and a depth of 0.4 m. Wave reflections are reduced by a passive wave absorption system [27]. A singular piston-type wavemaker at the upstream side of the flume can reproduce regular, irregular, and solitary waves up to 0.25 m for a maximum water depth of 0.7 m. The experiments were conducted using a geometric scale of 1:50 with incident waves propagating in the direction of the currents [28]. Currents were generated using two intake pipelines with a combined maximum flow capacity of 255 m^3/h, ensuring a depth-average mean flow velocity of up to 0.16 m/s for the target water depth d = 0.4 m. Tests also include regular/irregular "waves-only" conditions. Irregular waves were reproduced following JONSWAP spectra with a peak enhancement factor (Y) of 3.3, adopting a representation of North Sea conditions for all tests.

For the wave measurements, 4 wave gauges, sampled at 100 Hz, were placed along the flume to measure the water-free surface elevation at selected locations (Figure 1). Two gauges were placed on the seaside near the model to measure the local wave conditions, one on the leeward side to assess the effects of the oscillating surge WEC on the transmission coefficient, and one closer to the wavemaker. The gauge data allow the estimation of the wave-generated bottom orbital velocities (U_m) using a MATLAB (v.R2022b) routine [29], which is necessary to predict S_{3D} accurately. The reflection coefficients were determined for every test, using the incident and reflected wave heights, with values ranging from 0.10 to 0.17.

Current-induced flow velocities were measured through an Acoustic Doppler Velocimeter (ADV)—Vectrino+, Nortek AS, Rud, Norway. The ADV was placed in line with the wave gauges, 2.5 m upstream from the model (Figure 1). The ADV was installed vertically at 0.16 m (0.4d) above the flume ground level, sampled at 100 Hz, with the x-axis pointing in the current direction. Measurements were not made closer to the bed due to the ripple migration and the minimum distance required for a good signal quality of the ADV. Preliminary tests were carried out to adjust the intended Uc values without the influence of waves.

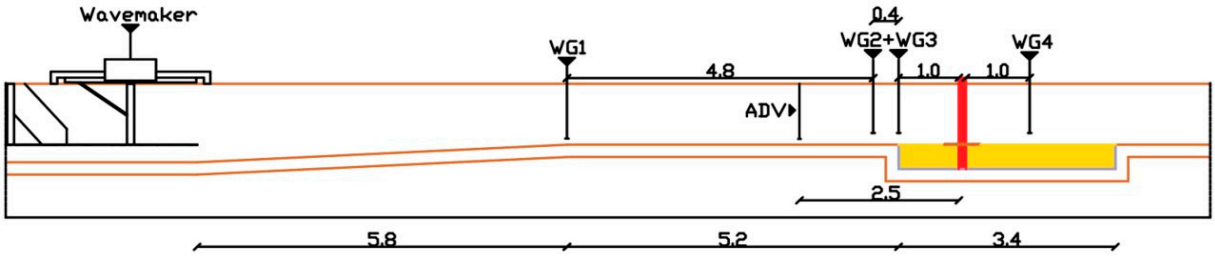


Figure 1. Experimental setup and wave gauge (WG) placement (dimensions in meters).

2.2. Model Layout

A monopile foundation was simulated by acrylic glass with a diameter (D_p) of 110 mm. The pile was positioned around 1 m from the beginning of the sediment box at a 12 m distance from the wavemaker (Figure 1). A circular-shaped dynamic scour protection model was designed [7,16], with a uniform thickness of 2.5 times the nominal median grain size (D_{n50}) and an overall diameter of 5 times the pile diameter (Figure 2). The material yields a D_{n50} = 3.696 mm for the armour layer, a density of ρ_s = 2.66 mg/m^3, and a D_{85}/D_{15} ratio of 3—very wide grading material [30]. Some stones were painted in different colours, creating mainly two concentric rings around the pile (Figure 3). The idea was to have an inner circle demarcating the amplification zone area and to allow a visual observation and distinction of the amount, direction, and displacement of the stones. A polypropylene geotextile with a surface density of 0.330 kg/m^2 and the same diameter as the armour layer was applied as a filter layer to avoid the washing out of the fine material. As for the sediment box, the sand used had a median diameter of d_{50} = 0.215 mm, a density of ρ_s = 2.59 mg/m^3, and a geometric standard deviation $\sigma_s = \sqrt{(d_{84}/d_{16})}$ = 1.8.

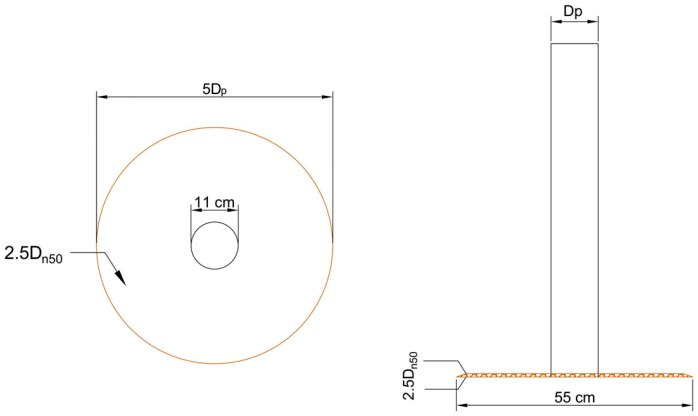


Figure 2. Monopile physical model scheme (Geometric scale: 1:50).



Figure 3. View of the scour protection (with demarcation of the amplification zone).

Regarding the WEC used to perform tests for a hybrid foundation, several devices could be suitable for testing. To assess and analyse the influence of a converter's oscillatory movement, it was decided to adapt and scale down a FOSWEC (floating oscillating surge wave energy converter) device [24–26]. This 6-degrees-of-freedom (DOF) floating WEC was designed, built, and tested at Oregon State University in a geometric scale of 1:33 to develop open-access datasets for validating numerical model codes and create an in-house device suitable for future experimental campaigns regarding marine renewable energy. The device comprises two flaps hinged to a central platform, containing a power take-off (PTO) system and two belt drive systems that operate the flaps. It also has two lateral buoys and openings on the top and bottom of the device (Figure 4).

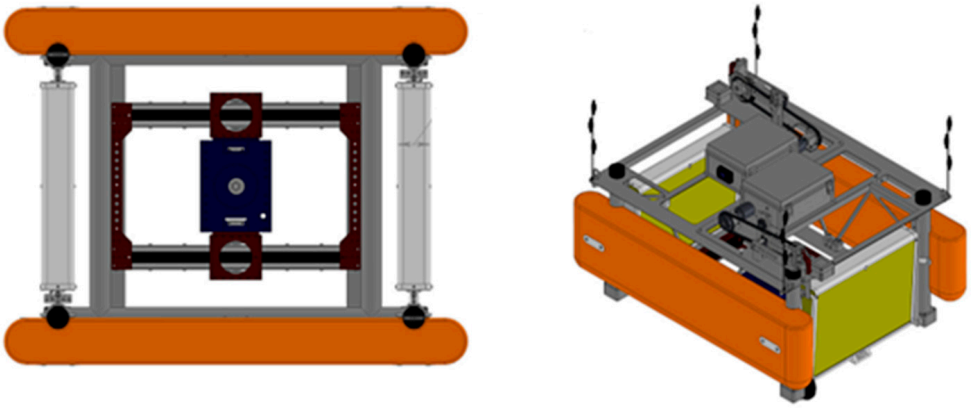


Figure 4. Original FOSWEC scheme [25], adapted and reprinted with permission from© 2020 Elsevier Ltd. (Amsterdam, The Netherlands).

The adapted model built for this study was a simplified version fixed to the monopile 15 cm above the sediment bed through two small cantilever arm braces (Figure 5), locking all the converter's body DOFs. Instead of a PTO system, a simplified system using springs was mounted, with a spring constant that limited the flaps' pitch to a maximum motion angle of $\pm 25°$, Figure 6, the same angle motion of the FOSWEC device [24]. The simplification and substitution of a fully functional PTO system using springs was made, since the primary goal of this study was to assess the impact of the device on the amplification and enhancement of the flow patterns, instead of evaluating the performance and efficiency of the converter's harvesting capacity under the proposed hydrodynamic conditions.



Figure 5. Oscillating surge WEC model construction and installation.

It is recommended to maintain the blockage ratio below the recommended threshold of 1/6 to minimise wall effects and avoid local acceleration of the flow in the contracted areas or excessive influence of the wall's friction in the hydrodynamics [14]. In the present study, the inherent constraints imposed by both the flume spacing and the necessity to maintain

the structural configurations and dimensions of the OSWEC led to a slight deviation of this ratio, as the device's overall form could not be appropriately scaled without compromising its wave–device interaction or the experimental setup. However, the region for higher blocking is placed at the superficial part of the water depth. Excluding the submerged part of the OSWEC at the monopile foundation, the ratio remained way below 1/6, i.e., 1/9. The model was carefully implemented to optimise the balance between achieving a realistic Froude-scaled setup and mitigating the potential blockage effect closer to the seabed to avoid the flow blockage near the protection. Therefore, for the region directly between the OSWEC's base and the sediment bed/scour protection, encompassing a 15 cm vertical distance, the blockage ratio was successfully maintained below the 1/6 mark. This ensured that the near-bed flow dynamics in this area, which are the most influential on the scour processes, were not influenced by the side wall effects. However, for the model's upper region, the considerations mentioned above and scaling led to a higher blockage ratio. It is acknowledged that this represents a study limitation and may lead to a localised acceleration of the flow and enhancement of streamflow contractions. However, it is essential to contextualise its potential impact on these research objectives. Since the focus was to assess scour damage occurring at the protection due to the oscillating movement of the WEC's paddles, which creates mainly a variation of upward/downward pressure right beneath the device in the scour protection region, enhancing downflow in an area where the blockage criterion was met. Therefore, while the hydrodynamics of the device's upper structure might be subject to some influence, it can be stated that the results regarding the scour damage in the protection remain representative. Future research could benefit from testing in larger-scale facilities to further minimise wall effects across the entire model and validate these findings. Nevertheless, the present study aimed to provide novel and valuable insights into the scour behaviour around hybrid foundations, highlighting critical interactions essential for effective design and understanding scour protections.

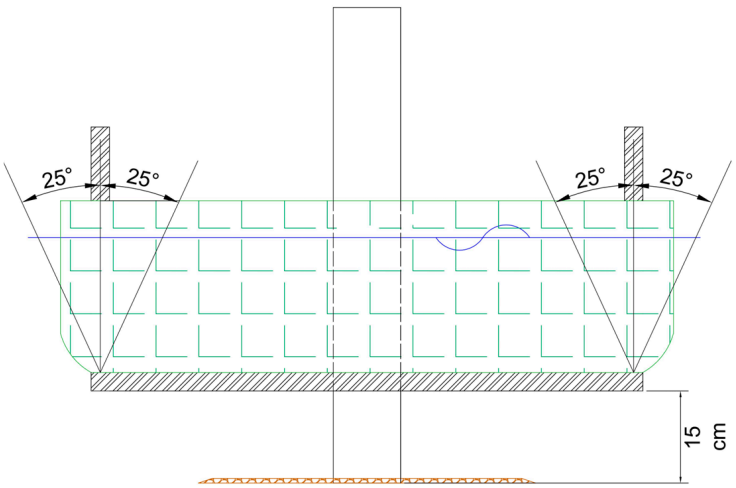


Figure 6. Oscillating surge WEC scheme (Geometric scale: 1:50).

2.3. Hydrodynamic Conditions and Scour Measurement Technique

The hydrodynamic conditions (Table 1) were selected to cover a specific range of wave–current ratios (U_{cw}) and KC numbers while considering other experimental campaigns found in the literature. Tests were run until 3000 waves, except in cases where the failure of the scour protection occurred prematurely. Three types of hydrodynamic conditions used for the monopile (M) and hybrid foundation (MH) were: irregular waves with currents in the same direction (WC), irregular waves only (WI), and regular waves only (WR). For the selected conditions and with the scour protection configuration, Table 2, it was expected to observe different behaviour from the scour protection (static, dynamic, or failure).

Table 1. Physical model hydrodynamic conditions (geometric scale: 1:50).

Test	Number of Waves	d [m]	H_s [m]	T_p [s]	U_m [m/s]	U_c [m/s]	U_{cw}	$S_{3D,predicted}$	MOB_{top}	KC_{Tot}
M_WC_7	3000	0.4	0.07	1.414	0.080	0.155	0.66	0.08	0.25	3.05
M_WC_11			0.11	1.697	0.143		0.52	0.63	0.41	4.66
M_WC_15.5			0.155	1.980	0.183	0.050	0.21	1.79	0.48	4.28
M_WI_14			0.14	2.263	0.208	-	0.00	3.43	0.53	4.39
M_WR_14			0.14 (Regular)							
MH_WC_7	3000	0.4	0.07	1.414	0.080	0.155	0.66	0.08	0.25	3.05
MH_WC_11			0.11	1.697	0.143		0.52	0.63	0.41	4.66
MH_WC_15.5			0.155	1.980	0.183	0.050	0.21	1.79	0.48	4.28
MH_WI_14			0.14	2.263	0.208	-	0.00	3.43	0.53	4.39
MH_WR_14			0.14 (Regular)							

Table 2. Physical model foundation and scour protection configuration (model values).

Geometric Scale: 1:50	
D_p (m)	0.11
D_{n50} (mm)	3.696
Armour Layer ρs (kg/m^3)	2666
Armour Thickness (t_s)	$2.5D_{n50}$
Armour Extent (D)	$5D_p$
Filter	Geotextile
D_{85}/D_{15}	3
MOB	0.25–0.53

To measure the seabed bathymetry and the scour of the protection, a FARO® focus laser scanner (2 million points/second, a 3D precision of 2 mm at 10 m, 1 mm standard deviation at 10 and 25 m) was used to obtain high-resolution 3D Digital Terrain Models (DTM). This technique allows the accurate representation of the erodible areas and the respective surroundings; thus, they were taken before and after each experimental test and wave train. The laser scan precision is smaller than the D_{n50} used in the scour protection, hence enabling a high-precision identification of all the armour layer units' movements, even spot deformations. The postprocessing of the DTMs was performed using the Autodesk ReCap and the CloudCompare software (v2.12.4). This resulted in precise point clouds of the seabed, scour protection, and hybrid structure profiles and contours. The DTMs were then used to assess scour depth and the $S_{3D,measured}$ values using a MATLAB routine [21] to employ the overlapping-circle technique. In addition, a visual observation and evaluation, plus a photographic register of all tests, were made to compare the results of the damage number obtained.

3. Experimental Results and Analysis

The experimental test campaign was planned so that the riprap protection and the controlled hydrodynamic conditions were aligned with the study performed by [7] for a more direct comparison of the results and to assess the impact and validation of using the overlapping-circle technique. A discussion of the measured results with the KC_{tot}-MOB_{top} prediction formula [22] was also performed. The results for both formulations differed from the predicted values, opening a meaningful discussion regarding the failure criterion and how scour damage is measured and evaluated.

3.1. Scour Damage (S_{3D})

For all the tests, the overlapping-circle technique was applied by using a $A_{sub} = 4D_{n50}^2$ and an overlapping distance of 50% [21], allowing an objective quantification of the scour protection damage under each test condition. Table 3 summarises all the measured conditions. The U_{cw} values distinguish the three wave-dominated tests ($U_{cw} < 0.44$) from the current-dominated tests ($U_{cw} > 0.44$) [31]. The novel method provided high-resolution representations of the scour patterns and high accuracy of the $S_{3D,measured}$ values and distribution (see Figures in Appendix A). As expected, and generally, S_{3D} correlates highly with the hydrodynamic load intensity. For low-energy conditions, the maximum $S_{3D,measured}$ values were lower and increased with higher wave heights. Also, when comparing the results of the wave-only tests (M_WI vs. M_WR and MH_WI vs. MH_WR), the S3D values were slightly higher when using regular waves, aligned with the findings of a study performed in rubble-mound structures [32], w attributed these difference to the fact that the root mean square (H_{rms}) value for irregular waves tends to be smaller than the wave height for regular waves.

Table 3. Experimental measured conditions for scour protection tests—model values.

Test	Number of Waves	H_s [m]	T_p [s]	U_m [m/s]	U_c [m/s]	U_{cw}	$S_{3D,predicted}$	$S_{3D,measured}$	Visual Classification
M_WC_7_1000	1000	0.072	1.471	0.085	0.157	0.65	0.06	1.43	Slightly Dynamic (all 3000 waves)
M_WC_7_2000	1000	0.073	1.471	0.086	0.157	0.65	0.07	2.11	
M_WC_7_3000	1000	0.073	1.471	0.086	0.157	0.64	0.08	1.95	
M_WC_11_1000	1000	0.100	1.613	0.126	0.156	0.55	0.48	1.73	Dynamic (all 3000 waves)
M_WC_11_2000	1000	0.104	1.613	0.131	0.158	0.55	0.57	1.63	
M_WC_11_3000	1000	0.111	1.613	0.140	0.157	0.53	0.63	1.83	
M_WC_15.5_1000	1000	0.155	2.083	0.223	0.048	0.18	1.79	2.87	Failure
M_WI_14_1000	1000	0.136	2.174	0.199	-	0.00	2.63	2.77	Dynamic (Almost failure, all 3000 waves)
M_WI_14_2000	1000	0.136	2.174	0.199			3.11	3.08	
M_WI_14_3000	1000	0.136	2.174	0.199			3.43	3.08	
M_WR_14_1000	1000	0.142	2.222	0.209	-	0.00	2.63	3.18	Failure (1000 waves)
M_WR_14_2000	1000	0.143	2.174	0.209			3.11	3.30	
M_WR_14_3000	1000	0.143	2.174	0.209			3.43	3.21	
MH_WC_7_1000	1000	0.074	1.299	0.078	0.156	0.67	0.06	1.97	Failure (2000 waves)
MH_WC_7_2000	1000	0.071	1.471	0.084	0.155	0.65	0.07	3.25	
MH_WC_7_3000	1000	0.070	1.471	0.083	0.157	0.65	0.08	2.86	
MH_WC_11_1000	1000	0.110	1.613	0.139	0.157	0.53	0.48	5.38	Failure
MH_WC_15.5_1000	1000	0.156	1.961	0.219	0.051	0.19	1.79	9.81	Failure
MH_WI_14_1000	1000	0.138	2.273	0.205	-	0.00	2.63	7.28	Failure
MH_WR_14_1000	1000	0.137	2.273	0.203	-	0.00	2.63	8.55	Failure

For the monopile tests (M_WC, M_WI, and M_WR), the scour protections exhibited lower damage rates across all the hydrodynamic conditions when compared to their hybrid structure counterparts (MH_WC, MH_WI, and MH_WR), as shown in Figures A1–A20 and Table 3, where very pronounced scour deformations were obtained for similar conditions.

In some cases, nearly double or triple the damage number from the corresponding monopile test was obtained, consistent with the intense sediment erosion, the washout of the armour layer material, and the considerable sinking of the seabed under the filter layer (Figure 7).

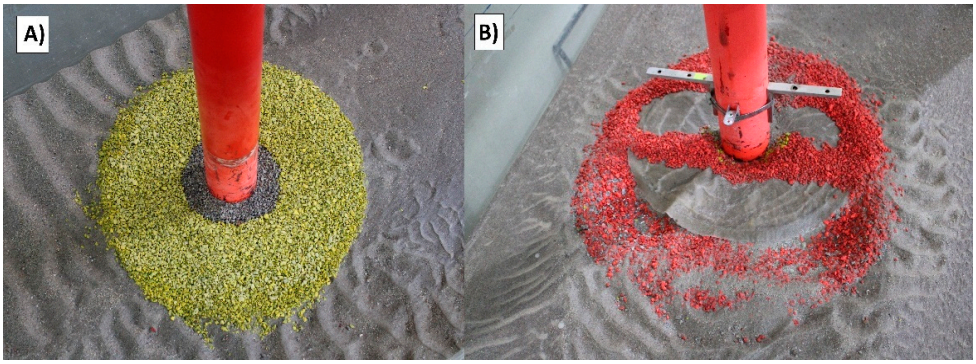


Figure 7. Damage comparison between the tests: (**A**) M_WR_14_1000 (monopile) and (**B**) MH_WR_14_1000 (hybrid monopile—test stopped due to large deformation of the armour layer and filter).

For most tests using a hybrid structure, failure occurred within the first 1000 waves. The only hybrid monopile test that provided scour protection support for some of the initial enhanced flow patterns was the MH_WC_7 test, which endured 2000 waves. The flow patterns responsible for the scour mechanism in monopiles are well documented [33]. However, with the results obtained for the hybrid structure, it is reasonable to assume that some of the main mechanisms responsible for scour were definitively enhanced. Due to the oscillatory movement of the paddles, on the front side of the foundation, the downflow was the flow pattern that caused most of the damage. Conversely, in the leeside, the movement of the downstream paddle enhanced the intensity of the lee–wake and counter-rotating vortices. Moreover, due to the dimensions of the WEC, the approaching flow conditions increase the streamline contractions around and beneath the device, which also adds to the overall result.

In contrast, monopiles retained integrity under mild conditions, M_WC_7 and M_WC_11, demonstrating dynamic behaviour unequivocally for the duration of the 3000 waves. For more intense conditions, the protection failed for M_WC_15.5 and M_WR_14 for the first 1000 waves. Although the regular wave-only test failed for the first wave train, the test was continued for comparison with the irregular wave test. The same was done for the hybrid test MH_WC_7, where failure occurred before the 3000-wave limit, but a final wave train was performed for comparison with the non-hybrid counterpart. Regarding the M_WI test, the high S_{3D} value suggested that the scour protection had failed. Still, when visually assessing damage using Figure 8 and comparing it to Figure A10, no distinctive filter exposure was observed despite intense movement of the armour layer units. Therefore, the protection was deemed to be on the edge between the dynamic behaviour and failure.

A noteworthy capacity of dynamic scour protections is to reshape and recover from a specific damage degree due to the allowed movement of the armour layer units [12]. That capacity was empirically observed during the experimental tests, most notably by the tests M_WC_7_2000 to M_WC_7_3000. Furthermore, this characteristic was also manifested in a protection where failure occurred, from MH_WC_7_2000 to MH_WC_7_3000, where a partial recovery from a significant damage rate (quantified as an S_{3D} reduction from 3.25 to 2.86) was observed. While both scenarios exhibit filter exposures, a subset of scour holes identified post-2000-wave train exposure was filled during the 3000-wave train. The backfilling originated from the armour layer units that had previously been displaced (Figure 9)—suggesting a potential for recovery under mild conditions. This observation

raises a pertinent question regarding the potential for scour protections to recover and turn back to dynamic stability after failure.



Figure 8. M_WI_14_3000 test scour protection.

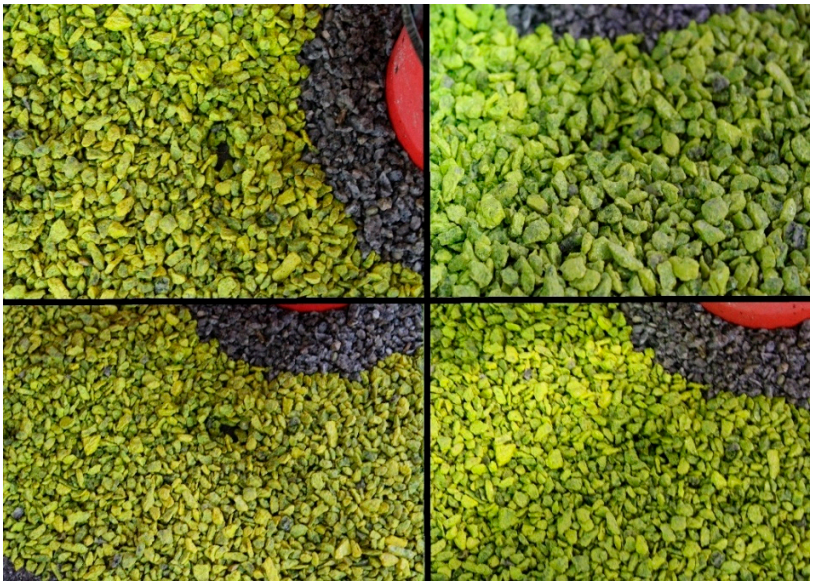


Figure 9. Scour holes (MH_WC_7_2000—**left**) and refilling (MH_WC_7_3000—**right**).

A discrepancy is visible when comparing the $S_{3D,measured}$ with those predicted by using Equation (5) formula (Table 3). It can be observed that, in general, the formula underestimates scour for the conditions tested. This is aggravated when dealing with a hybrid structure. The formula underestimates actual damage, suggesting that the formula needs to incorporate other non-linear factors that may occur in more complex or hybrid systems. However, this underestimation also stems from methodological differences in how damage is measured by the approaches developed by [7,21]. As previously mentioned, the methodology established by [7] makes use of fixed sub-areas equivalent to the monopile cross-section, which averages the scour depth over larger areas. Moreover, it does not consider the thickness of the scour protection.

Hence, if the damage number represents the number of protection layers lost to scour as a function of D_{n50}, as indicated by [7], for the model thickness ($t_s = 2.5D_{n50}$), an $S_{3D} = 1.0$ will not be a valid representation that physically failure occurs. Even dynamically stable scour protections were observed by [7,20], for S_{3D} values larger than 1.0, up to 1.25, thus showing that the reference values proposed by [7] can be conservative. On the contrary, the approach developed by [21] allows the use of the criterion of failure suggested by [12], as

the sub-area to be analysed over an overlapping mesh created over the protection. Thus, for a selected A_{sub}, in this case $4D_{n50}^2$, the filter layer exposure and failure should at least occur only when $S_{3D} \times D_{n50} \geq t_s$. Considering this, a comparison of S_{3D} and thickness as a function of D_{n50} could be more informative. Consequently, the failure limit should not be a fixed threshold value independent of the protection thickness, such as $S_{3D} = 1.0$, as proposed by [7], but a range around $S_{3D} = n_s$ for $t_s = n_s \cdot D_{n50}$, accounting for a degree of uncertainty, being that ns is the number of rock stone size layers [18].

By adopting this perspective, comparing $S_{3D,measured}$ values to a starting point of $S_{3D,failure} = 2.5$, determined by the n_s value used during the experimental tests, allows for a clearer visual interpretation of the scour protection's behaviour as a function of the damage number measured using the overlapping method and a more straightforward understanding of the physical meaning of the S_{3D}—see Figures 10–12. The static limit of $S_{3D} = 0.25$ was maintained, as in the research carried out by [7]. It is worth reiterating that for the M_WI test, the values obtained for the damage number, in fact, point to failure for the totality of the 3000 waves, even for $S_{3D,failure} = 2.5$. This reinforces the idea that the boundary between scour behaviour classification should be defined by a range that accounts for a certain degree of uncertainty instead of a single fixed threshold value.

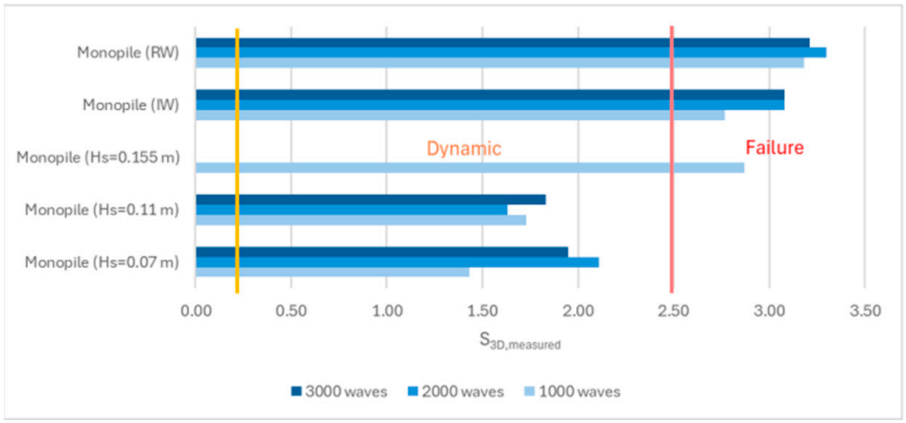


Figure 10. S3D and damage classification for new limits based on the thickness of the scour protection—monopile tests.

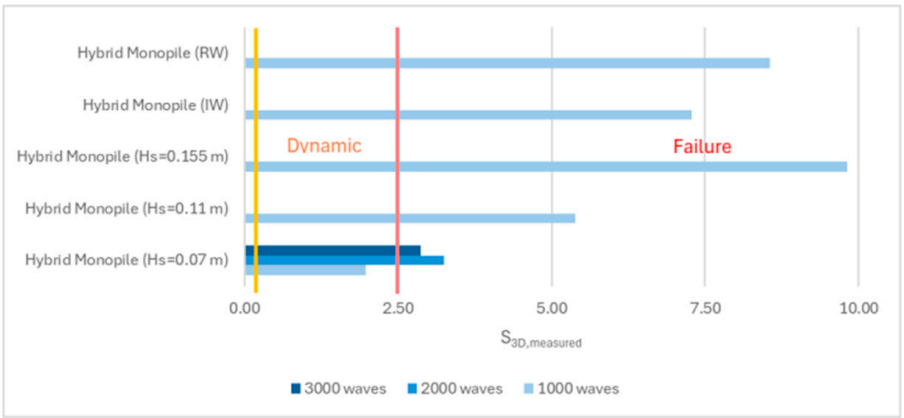


Figure 11. S3D and damage classification for new limits based on the thickness of the scour protection—hybrid monopile tests.

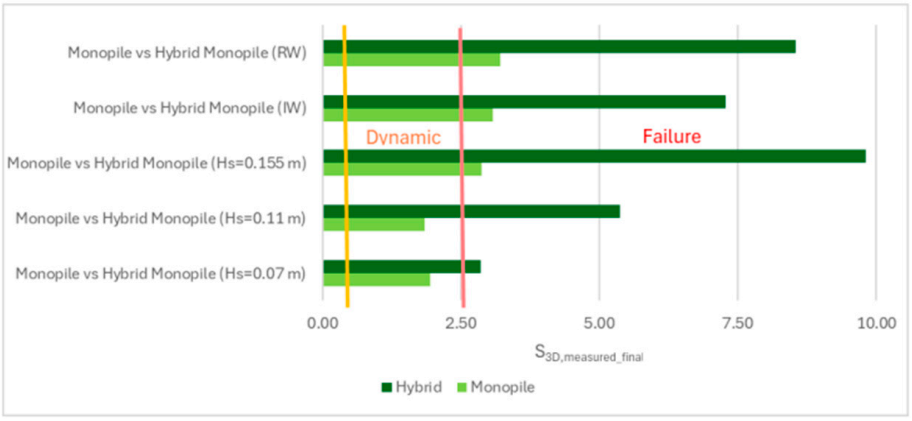


Figure 12. Comparison of S3D values between the monopile and hybrid monopile for the same hydrodynamic conditions.

As a side note, it was detected that in some of the tests (M_WC_7, M_WR, and MH_WC_7), the damage number reached a peak value around 2000 waves and subsequently decreased slightly for 3000 waves or even remained constant in the M_WI test series. This observation highlights that most damage occurs in the first 1000 waves, as observed by [18]. Thereafter, scour holes begin to backfill with surrounding material, after 3000 or even 5000 waves, while other holes may appear, indicating an equilibrium state within this interval.

The development of a design formula combining scour depth, area, and volume, with guidelines on the volume–area–depth relationship, was raised by [22]. A generalisation of the scour volume–area–depth relation, assuming a S_{3D} value for a $A_{sub} = n_s D_{n50}^2$, is given by applying the methodology by [21]:

$$\frac{V_e}{A_{sub}} = S = S_{3D} \times D_{n50} \tag{11}$$

$$\frac{V_e}{S} = A_{sub} = n_s \cdot D_{n50}^2 \tag{12}$$

$$\frac{A_{sub}}{S} = (n_s \cdot D_{n50})/S_{3D} \tag{13}$$

Moreover, assessing the ratio S/D_p is a widespread practice in the literature when analysing scour rates for unprotected structures. Conversely, determining the deformation for riprap scour protections becomes expendable, since S/D_p becomes reduced, in some cases residual, and does not help the interpretation of the state of the protection. Taking this into consideration and due to the limitations of the fixed sub-areas approach [7], a new ratio was introduced by [18], the damage increase ratio ($\Delta S_{3D}/n_s$), to express the variation of damage between each wave train, while considering the thickness of the scour protection layer by using the number of rock stone sizes. The experimental test results determined a specific range of values of the damage increase ratio for each scour protection behaviour (static, dynamic, failure) for three different durations (0 to 1000 waves, 1000 to 3000 waves, and 3000 to 5000 waves):

- From 0 to 1000 waves: $\Delta S_{3D}/n_s$ = [0.05–0.09] (static), $\Delta S_{3D}/n_s$ = [0.07–0.39] (dynamic), $\Delta S_{3D5000}/n_s$ = [0.19–0.42] (failure).
- From 1000 to 3000 waves: $\Delta S_{3D}/n_s$ = [0.00–0.03] (static), $\Delta S_{3D}/n_s$ = [0.00–0.12] (dynamic), $\Delta S_{3D}/n_s$ = [0.00–0.50] (failure).
- From 3000 to 5000 waves: $\Delta S_{3D}/n_s$ = [−0.02–0.01] (static), $\Delta S_{3D}/n_s$ = [−0.01–0.07] (dynamic), $\Delta S_{3D}/n_s$ = [−0.04–0.17] (failure).

By comparing the values in Table 4, most damage occurs for the first 1000 waves, but at higher rates than the ones proposed by [18]. However, for the 1000 to 3000 wave duration, the values align with the suggested range. By looking strictly for the ratio values, it is possible to determine the speed and rate at which scour damage is developing, but it is hard to determine in which condition and/or behaviour the protection is. Therefore, instead of using the S/D_p and the $\Delta S_{3D}/n_s$ ratio, which do not have a clear physical meaning and can be unclear, and in the case of the $\Delta S_{3D}/n_s$ ratio has overlapping ranges for different behaviours, this study proposes a slight adaptation: S/D_p into S/t_s and $\Delta S_{3D}/n_s$ into S_{3D}/n_s, both for a certain A_{sub} (or $A_{failure}$).

Table 4. Damage increase ratio results $\Delta S_{3D}/n_s$.

Test	Visual Classification	$\Delta S_{3D}/n_s$
M_WC_7_1000 M_WC_7_2000 M_WC_7_3000	Slightly Dynamic	0.57 (0–1000 waves) 0.21 (1000–3000 waves)
M_WC_11_1000 M_WC_11_2000 M_WC_11_3000	Dynamic	0.69 (0–1000 waves) 0.04 (1000–3000 waves)
M_WC_15.5_1000	Failure	1.15
M_WI_14_1000 M_WI_14_2000 M_WI_14_3000	Dynamic (Almost Failure)	1.11 (0–1000 waves) 0.12 (1000–3000 waves)
M_WR_14_1000 M_WR_14_2000 M_WR_14_3000	Failure	1.27 (0–1000 waves) 0.01 (1000–3000 waves)
MH_WC_7_1000 MH_WC_7_2000 MH_WC_7_3000	Failure	0.79 (0–1000 waves) 0.36 (1000–3000 waves)
MH_WC_11_1000	Failure	2.15
MH_WC_15.5_1000	Failure	3.92
MH_WI_14_1000	Failure	2.91
MH_WR_14_1000	Failure	3.42

These slight modifications convert both into more practical, intuitive ratios and are more representative of the scour protection deformation state and the relative amount of armour layer thickness loss. For these ratios, the authors suggest that the limits proposed by [7], 0.25 for static behaviour and 1.0 for failure, could make more sense as a good starting point than for the S_{3D}:

- S_{3D}/n_s *or* $S/t_s > 1$: failure–filter layer exposed, loss of filter layer and/or seabed lowering;
- $0.25 < S_{3D}/n_s$ *or* $S/t_s < 1$: dynamic behaviour—loss of thickness in the armour layer and/or movement of the armour layer units;
- $0 < S_{3D}/n_s$ *or* $S/t_s < 0.25$: static behaviour—no movement, or residual movement, of armour layer units;

- S_{3D}/n_s *or* $S/t_s < 0$: accretion of sediments around the armour layer unit;

For most tests, a variable limit for the damage number and the S/t_s ratio was used to fit the classification and assessment of the scour protection behaviour for the entire experimental campaign. The protections where failure was detected visually or with the overlapping-circle method correspond to values of $S_{3D} > 2.5$ or $S/t_s > 1.0$ (Table 5, Figures 10, 11 and 13). The same occurs for protections classified as dynamic, where $S_{3D} < 2.5$ or $S/t_s < 1.0$, with the only exception being the M_WI test, for the previously mentioned reasons. Therefore, it is worth mentioning that a failure criterion based on the S_{3D}/n_s or S/t_s is defined by the scour protection properties and geometry and is independent of the foundation used. Possible higher values obtained for hybrid foundations are not an indicator to redefine the failure threshold criterion but an indicator of increased scour damage that eventually should lead to the necessity to upgrade the characteristics of the scour countermeasure. In the end, the overlapping method proved to be valuable in visualising, tracking, and identifying the scour patterns, holes, rate, and consequently the assessment and quantification of the damage and behaviour of each scour protection tested.

Table 5. Scour depth, S_{3D}/n_s, S/t_s, and scour damage comparison.

Test	S [mm]	S/t_s S_{3D}/n_s	S/t_s S_{3D}/n_s (Failure)	$S_{3D,measured}$	$S_{3D,failure}$
M_WC_7_1000	5.29	0.57		1.43	
M_WC_7_2000	7.80	0.84		2.11	
M_WC_7_3000	7.21	0.78		1.95	
M_WC_11_1000	6.39	0.69		1.73	
M_WC_11_2000	6.02	0.65		1.63	
M_WC_11_3000	6.76	0.73		1.83	
M_WC_15.5_1000	10.61	1.15	1.0	2.87	2.5
M_WI_14_1000	10.24	1.11		2.77	
M_WI_14_2000	11.38	1.23		3.08	
M_WI_14_3000	11.38	1.23		3.08	
M_WR_14_1000	11.75	1.27		3.18	
M_WR_14_2000	12.20	1.32		3.30	
M_WR_14_3000	11.86	1.28		3.21	
MH_WC_7_1000	7.28	0.79		1.97	
MH_WC_7_2000	12.01	1.30		3.25	
MH_WC_7_3000	10.57	1.14		2.86	
MH_WC_11_1000	19.88	2.15	1.0	5.38	2.5
MH_WC_15.5_1000	36.26	3.92		9.81	
MH_WI_14_1000	26.91	2.91		7.28	
MH_WR_14_1000	31.60	3.42		8.55	

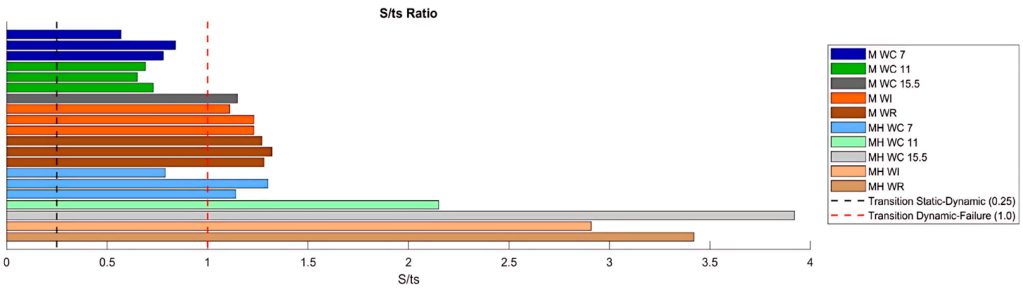


Figure 13. S/t_s ratio values and transition thresholds.

3.2. Overlapping Grid Ratio

It was proven by [21] that the damage number strongly depends on the grid ratio. However, the analysis of the volumetric damage concerning the grid ratio and the convergence between the two variables was made only for two large-scale cases. To expand and compare its dataset with the tests performed during this study, an analysis of the $S_{3D,max}$ results for each test for different $\eta_{S3D,grid}$ was performed. Moreover, since the maximum damage number is valid only for a single value at the deepest point of the scour protection, a statistical study on the development of the standard deviation and the 95% percentile of the S_{3D} was implemented to verify a possible convergence stage.

The grid ratios were selected to cover a variety of A_{sub} values, including the monopile cross section [7], $25D_{n50}^2$ (corresponding to five armour layer units), $4D_{n50}^2$ as in [12], and many others equivalent to the arrangement of multiple or even single armour layer units ($n\mathrm{D_{n50}} \times n\mathrm{D_{n50}}$) (Figure 14).

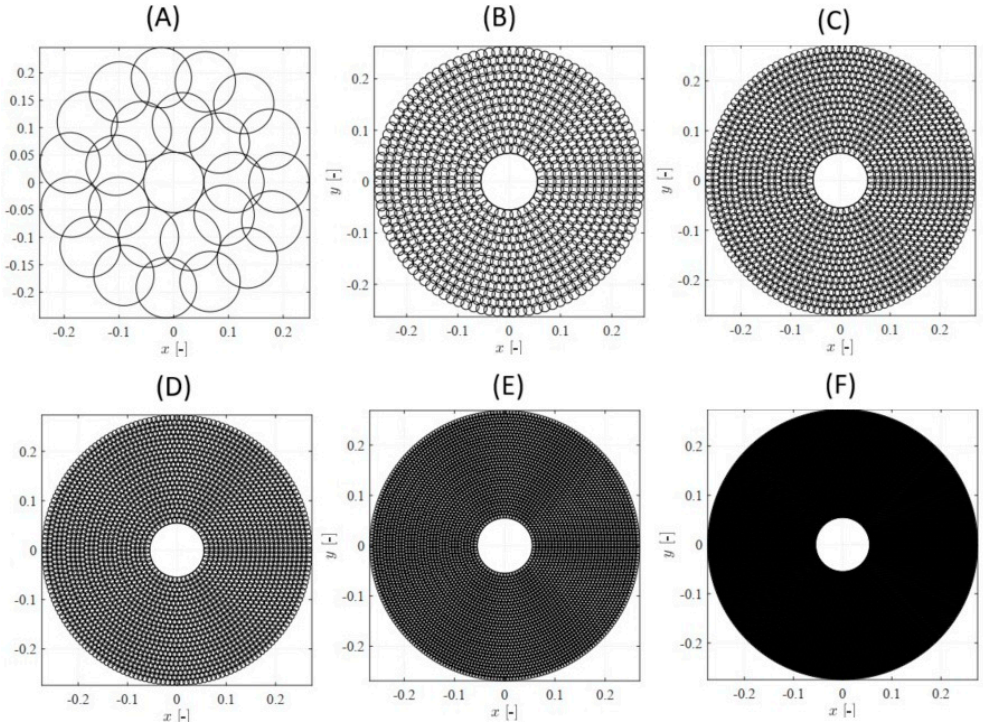


Figure 14. Overlapping-circle arrangement for different $\eta_{S3D,grid}$ and sub-areas: (**A**) $\eta_{S3D,grid} = 1.43 \times 10^{-3}$, $A_{sub} = A_{pile}$; (**B**) $\eta_{S3D,grid} = 1/25$, $A_{sub} = 25D_{n50}^2$; (**C**) $\eta_{S3D,grid} = 1/16$, $A_{sub} = 16D_{n50}^2$; (**D**) $\eta_{S3D,grid} = 1/9$, $A_{sub} = 9D_{n50}^2$; (**E**) $\eta_{S3D,grid} = 1/4$, $A_{sub} = 4D_{n50}^2$; (**F**) $\eta_{S3D,grid} = 1$, $A_{sub} = D_{n50}^2$.

Varying the grid ratio implies a variation in the number of elements, leading to a considerable variation in the maximum value of the damage number. Figure 15 illustrates the case for the M_WC_11_3000 tests. For higher grid ratios, i.e., lower A_{sub} and more sub-areas, the scour pattern becomes closer to the DTM representation. The figure also illustrates the considerable variation of outcomes for different ratios, where for an A_{sub} equal to the cross section of the monopile, the least amount of analysed elements, the maximum damage number detected was negative (accretion of sediments). Conversely, for an A_{sub} equal to a single armour layer unit (D_{n50}^2), S_{3D} was superior to the $S_{3D,failure} = 2.5$ (representative of a meaningless spot deformation in depth).

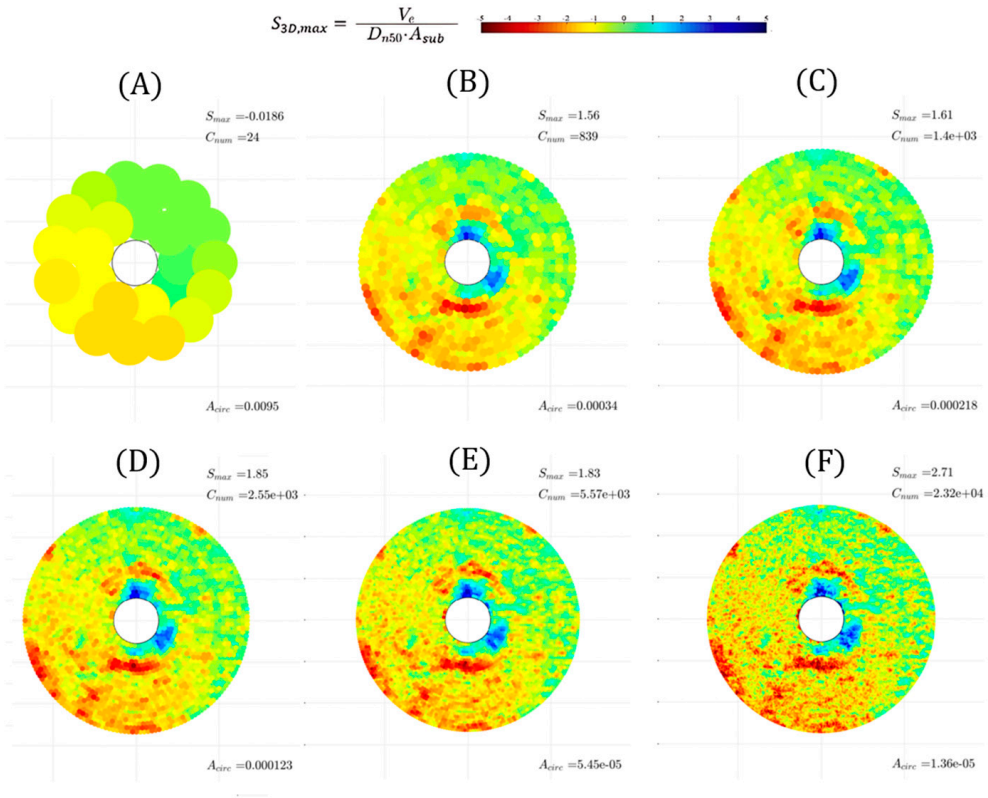


Figure 15. Influence of $\eta_{S3D,grid}$ on $S_{3D,max}$ value for test M_WC_11_3000: (**A**) $\eta_{S3D,grid} = 1.43 \times 10^{-3}$, $A_{sub} = A_{pile}$; (**B**) $\eta_{S3D,grid} = 1/25$, $A_{sub} = 25D_{n50}^2$; (**C**) $\eta_{S3D,grid} = 1/16$, $A_{sub} = 16D_{n50}^2$; (**D**) $\eta_{S3D,grid} = 1/9$, $A_{sub} = 9D_{n50}^2$; (**E**) $\eta_{S3D,grid} = 1/4$, $A_{sub} = 4D_{n50}^2$; (**F**) $\eta_{S3D,grid} = 1$, $A_{sub} = D_{n50}^2$.

The results obtained for the $S_{3D,max}$ vs. $\eta_{S3D,grid}$ for all the tests in the study (Tables A1 and A2) were plotted onto Figure 16 (monopile) and Figure 17 (hybrid monopile). Both plots show similar conclusions as in [21], a very strong dependency and positive correlation of the damage number with the grid ratio and/or size of the sub-area selected, demonstrating that different grid ratios lead to completely different results that would lead to entirely different interpretations of the scour protection behaviour. This is an argument for the necessity of considering a uniform criterion of failure to evaluate the performance of scour protections [21].

By comparing the results and the plots, it is evident that the $S_{3D,max}$ exponentially grows until approximately $\eta_{S3D,grid} = 1/10$ ($A_{sub} = 10D_{n50}^2$). The values seem to stabilise from that grid ratio value until $\eta_{S3D,grid} = 1/4$ ($A_{sub} = 4D_{n50}^2$) and from that point forward starts to increase linearly for cases where the scour damage was quantitatively lower (monopiles), opposite to cases where the damage was significant (hybrid monopile), where the $S_{3D,max}$ value appears to remain almost the same independently form the A_{sub} selected. Nevertheless, from the results obtained, the best range of grid ratios and sub-area to accurately assess the damage number value, for both cases, seems to be situated between $\eta_{S3D,grid} = 1/6$ ($A_{sub} = 6D_{n50}^2$) and $\eta_{S3D,grid} = 1/4$ ($A_{sub} = 4D_{n50}^2$), where residual or almost no differences were observed. These results indicate that the failure criterion $4D_{n50}^2$, Ref. [12] is a reasonable limit to correctly identify failure in a scour protection and an accurate A_{sub} to use on the overlapping method [21].

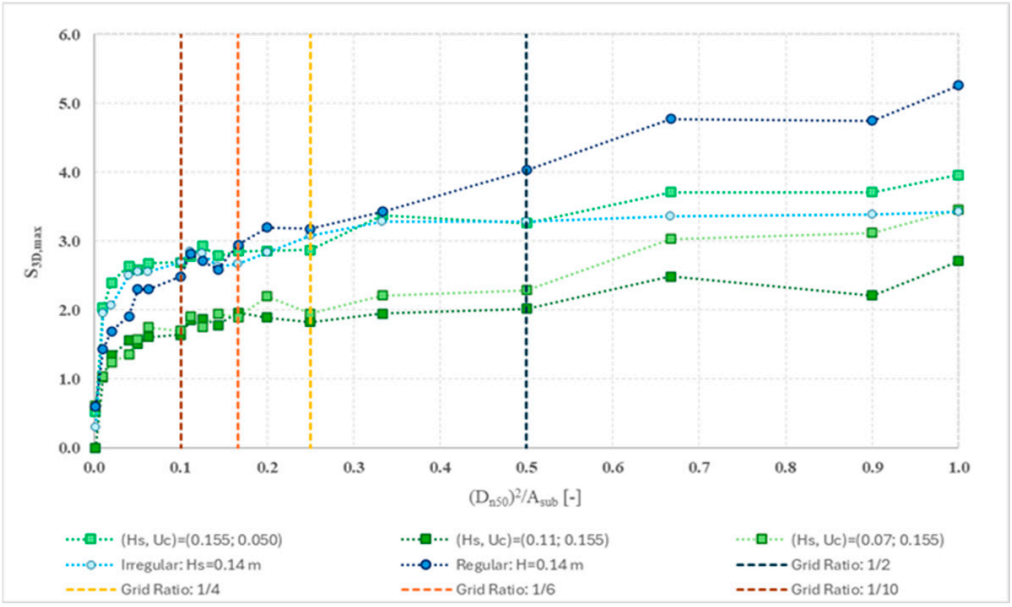


Figure 16. Variation of $S_{3D,max}$ with $\eta_{S3D,grid}$—monopile tests.

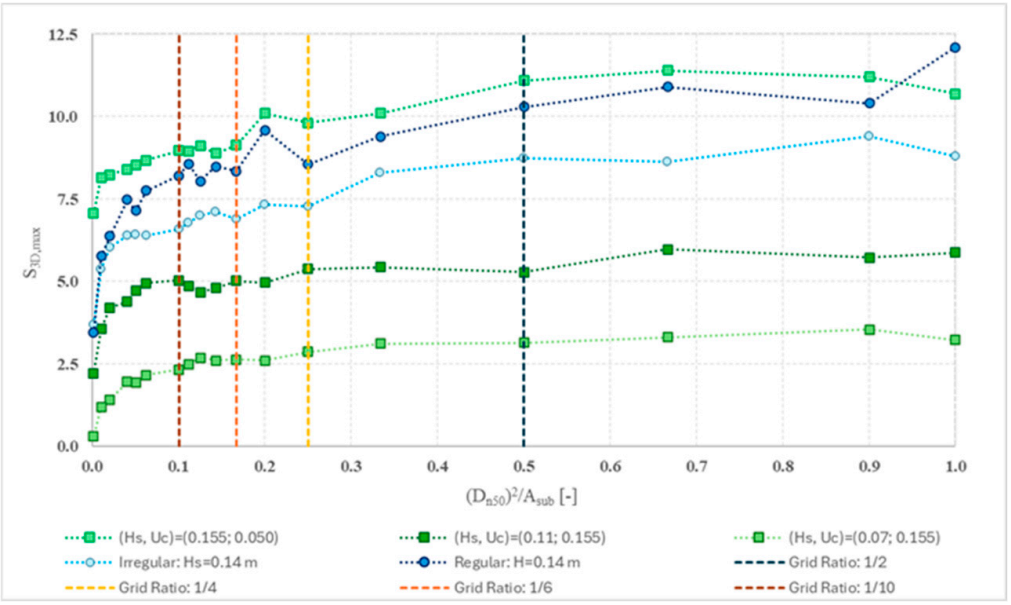


Figure 17. Variation of $S_{3D,max}$ with $\eta_{S3D,grid}$—hybrid monopile tests.

Since $S_{3D,max}$ seems to be fairly affected by the variation of the grid ratio and affected by minimal changes [21], the standard deviation (Figure 18) and the 95% percentile (Figure 19) of all $S_{3D,sub}$ values for each test were plotted to ensure if the convergence is given for the different grid ratios selected. For both statistical measures, $S_{3D,max}$ vs. $\eta_{S3D,grid}$ for all the tests in the study (Tables A1 and A2) were plotted onto Figure 16 (monopile) and Figure 17 (hybrid monopile). Both plots show similar conclusions as in the study performed by [21], a very strong dependency and positive correlation of the damage number with the grid ratio and /or size of the sub-area selected, demonstrating that different grid ratios lead to completely different results that would lead to entirely different interpretations of the scour protection behaviour. This is an argument for the necessity of considering a uniform criterion of failure to evaluate the performance of scour protections.

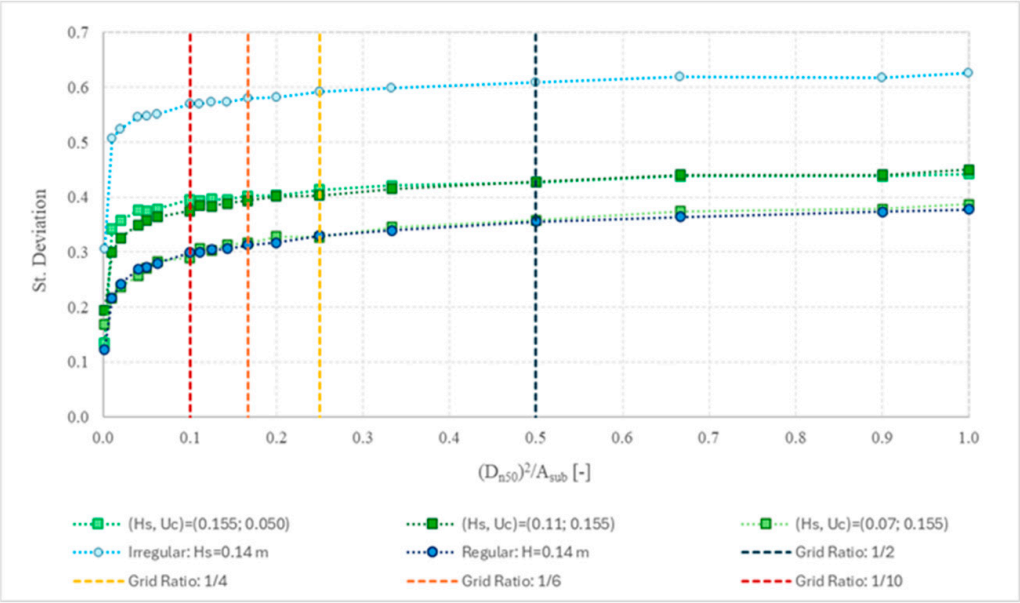


Figure 18. Variation of the standard deviation of $S_{3D,sub}$ with $\eta_{S3D,grid}$—monopile tests.

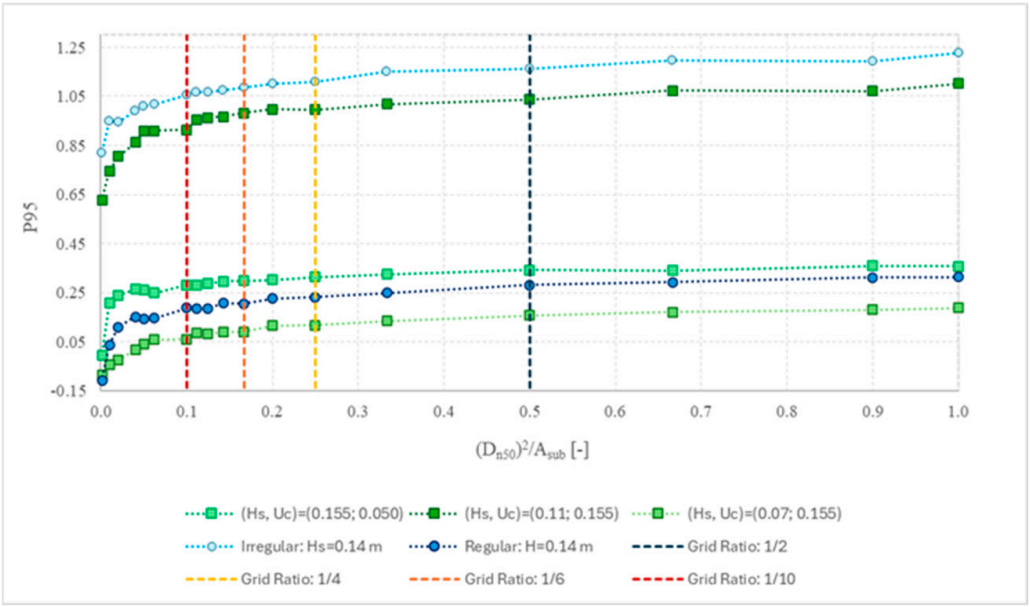


Figure 19. Variation of the 95% percentile (P95) of $S_{3D,sub}$ with $\eta_{S3D,grid}$—monopile tests.

3.3. KC_{tot}—MOB_{top} Effect and U_{cw} Analysis

In this section, the performance of the scour protection is evaluated using the dimensionless parameters MOB_{top} and KC_{tot}, based on a predictive model developed by [22]. While the proposed formula has proven effective in characterising scour deformation in conventional monopile foundations, its application to hybrid structures was not considered. The MOB_{top}-KC_{tot} framework was considered as having a higher correlation with scour depth and being the best absolute performance evaluator/predictor of a scour protection when compared to the stab parameter or the S_{3D} [22]. However, the calculation of the absolute and dimensionless predicted scour depths (S and S/D_p, respectively) using Equation (9) showed a consistent underestimation for the monopile values measured 2 to 7 times higher than the predicted (Table 6). Similar trends were observed in the hybrid monopile tests, where actual scour depths exceeded the predictions by factors of 7 up to 11.

Table 6. Scour measured vs. predicted values: KC_{tot}—MOB_{top} design formula [22].

Test	Number of Waves	S [mm]	$S_{predicted}$ [mm]	S/D_p	$S_{predicted}/D_p$	KC_{tot}	MOB_{top}
M_WC_7_1000	1000	5.29	1.10	0.048	0.010	3.27	0.26
M_WC_7_2000	1000	7.80	1.10	0.071	0.010	3.29	0.26
M_WC_7_3000	1000	7.21	1.10	0.066	0.010	3.29	0.26
M_WC_11_1000	1000	6.39	2.31	0.058	0.021	4.19	0.36
M_WC_11_2000	1000	6.02	2.64	0.055	0.024	4.29	0.38
M_WC_11_3000	1000	6.76	3.08	0.061	0.028	4.42	0.41
M_WC_15.5_1000	1000	10.61	7.59	0.096	0.069	5.25	0.62
M_WI_14_1000	1000	10.24	3.96	0.093	0.036	4.04	0.51
M_WI_14_2000	1000	11.38	3.96	0.103	0.036	4.04	0.51
M_WI_14_3000	1000	11.38	3.96	0.103	0.036	4.04	0.51
M_WR_14_1000	1000	11.75	4.73	0.107	0.043	4.33	0.54
M_WR_14_2000	1000	12.20	4.73	0.111	0.043	4.24	0.55
M_WR_14_3000	1000	11.86	4.73	0.108	0.043	4.24	0.55
MH_WC_7_1000	1000	7.28	0.99	0.066	0.009	2.79	0.25
MH_WC_7_2000	1000	12.01	1.10	0.109	0.010	3.23	0.25
MH_WC_7_3000	1000	10.57	1.10	0.096	0.010	3.24	0.25
MH_WC_11_1000	1000	19.88	3.08	0.181	0.028	4.40	0.41
MH_WC_15.5_1000	1000	36.26	7.04	0.330	0.064	4.92	0.63
MH_WI_14_1000	1000	26.91	4.40	0.245	0.040	4.35	0.52
MH_WR_14_1000	1000	31.60	4.29	0.287	0.039	4.31	0.51

In a first analysis, these discrepancies may be attributed to the fact that the methodology proposed by [22] relied on a different algorithm [23] to detect deformations and measure scour depths, $A_{sub} = 20D_{50}^2$, that may dilute the localised scour effects when compared to the overlapping-circle method ($A_{sub} = 4D_{n50}^2$). Additionally, the research developed by [22] used larger monopiles—D_p = 0.15 to 0.30 m vs. 0.11 m (model values)—different scour protection configurations—t_s = [1,2] D_{n50} vs. $t_s = 2.5D_{n50}$, extent of $3D_p$ vs. $5D_p$, ρ_s = [2650–3200] kg/m^3 vs. ρ_s = 2666 kg/m^3, and D_{85}/D_{15} = [1–3] vs. $D_{85}/D_{15} = 3$—and different model scales. Furthermore, the dataset (20 test points) in this experimental study was sparse when compared to the 380 tests performed by [22].

When a more detailed analysis was carried out, a crucial aspect was identified as a possible contribution to the discrepancy in the prediction values—the gradation width of the armour layer material. As Equation (2) was adopted by [22] to calculate the critical Shields parameter, the protection model in this study is considered a very wide-graded scour protection ($D_{85}/D_{15} = 3$). For this type of scour protection, a lower value of θ_{cr} is recommended by [15] for calculating the stab parameter, which is the same parameter as the MOB [22]. For both foundations, improvements were detected by recalculating the $S_{predicted}/D_p$ with the recommended value $\theta_{cr} = 0.035$ (Table 7 and Figure 20).

For the monopile, despite most values still falling short of accurately predicting the measured results, a substantial improvement was identified—S/D_p values for the M_WC_11, M_WI, and M_WR tests were underpredicted by factors of less than 1.5, while the S/D value for the M_WC_15.5 test was even overpredicted—see Figure 21. Focusing on the results obtained for the hybrid monopiles, the differences between the predicted and the measured S/D_p decreased, but the prediction was still considerably far from the measured scour depths (Table 7, Figures 20 and 21).

The pronounced underprediction values observed for the hybrid foundation (Table 7, Figures 20 and 22), regardless of the θ_{cr} used to determine the MOB_{top}, cannot be solely attributed to the omission of the gradation width in the formula. Rather, it can be reasonably assigned to the presence of the WEC and its major influence on scour. Equation (8) was not developed to capture WEC-induced flow amplifications and associated shear stress

increments generated by the paddles' motion—effects absent from the conditions used to derive the formulation. As the MOB_{top} measures the hydraulic loading relative to the armour layer resistance, its variation depends not only on the stability of the protection but also on changes in the flow patterns. As the KC_{tot} variable measures the contribution of wave-orbital and steady-current velocities relative to the structure, the WEC's paddle motion, by enhancing the flow patterns acting on the foundations, is expected to exert a pronounced effect on both parameters, sufficient to substantially increase the bed shear stress acting on the scour protection to well above the θ_{cr} of the armour layer material. That contribution is not expressed in the formula by means of an amplification or safety factor, leading to a massive underestimation of the predicted scour depth.

Table 7. Comparison of the predicted values using different critical Shields parameters.

Test	Number of Waves	S [mm]	S/D_p	$S_{predicted}$ [mm]	$S_{predicted}/D_p$	$S_{predicted}$ [mm]	$S_{predicted}/D_p$
				Θ_{cr} = 0.035		Θ_{cr}—Equation (2)	
M_WC_7_1000	1000	5.29	0.048	1.98	0.018	1.10	0.010
M_WC_7_2000	1000	7.80	0.071	1.98	0.018	1.10	0.010
M_WC_7_3000	1000	7.21	0.066	1.98	0.018	1.10	0.010
M_WC_11_1000	1000	6.39	0.058	4.18	0.038	2.31	0.021
M_WC_11_2000	1000	6.02	0.055	4.73	0.043	2.64	0.024
M_WC_11_3000	1000	6.76	0.061	5.72	0.052	3.08	0.028
M_WC_15.5_1000	1000	10.61	0.096	14.30	0.130	7.59	0.069
M_WI_14_1000	1000	10.24	0.093	7.48	0.068	3.96	0.036
M_WI_14_2000	1000	11.38	0.103	7.48	0.068	3.96	0.036
M_WI_14_3000	1000	11.38	0.103	7.48	0.068	3.96	0.036
M_WR_14_1000	1000	11.75	0.107	9.02	0.082	4.73	0.043
M_WR_14_2000	1000	12.20	0.111	8.80	0.080	4.73	0.043
M_WR_14_3000	1000	11.86	0.108	8.80	0.080	4.73	0.043
MH_WC_7_1000	1000	7.28	0.066	1.87	0.017	0.99	0.009
MH_WC_7_2000	1000	12.01	0.109	1.98	0.018	1.10	0.010
MH_WC_7_3000	1000	10.57	0.096	1.98	0.018	1.10	0.010
MH_WC_11_1000	1000	19.88	0.181	5.72	0.052	3.08	0.028
MH_WC_15.5_1000	1000	36.26	0.330	13.09	0.119	7.04	0.064
MH_WI_14_1000	1000	26.91	0.245	8.47	0.077	4.40	0.040
MH_WR_14_1000	1000	31.60	0.287	7.92	0.072	4.29	0.039

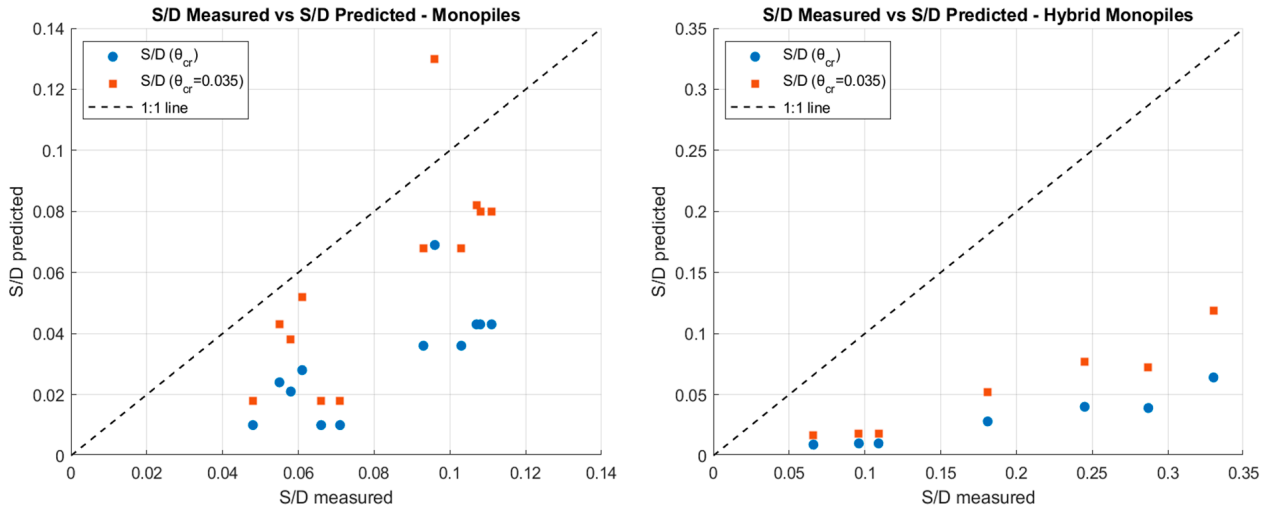


Figure 20. Comparison between measured vs. predicted S/D_p, using different values for θ_{cr}.

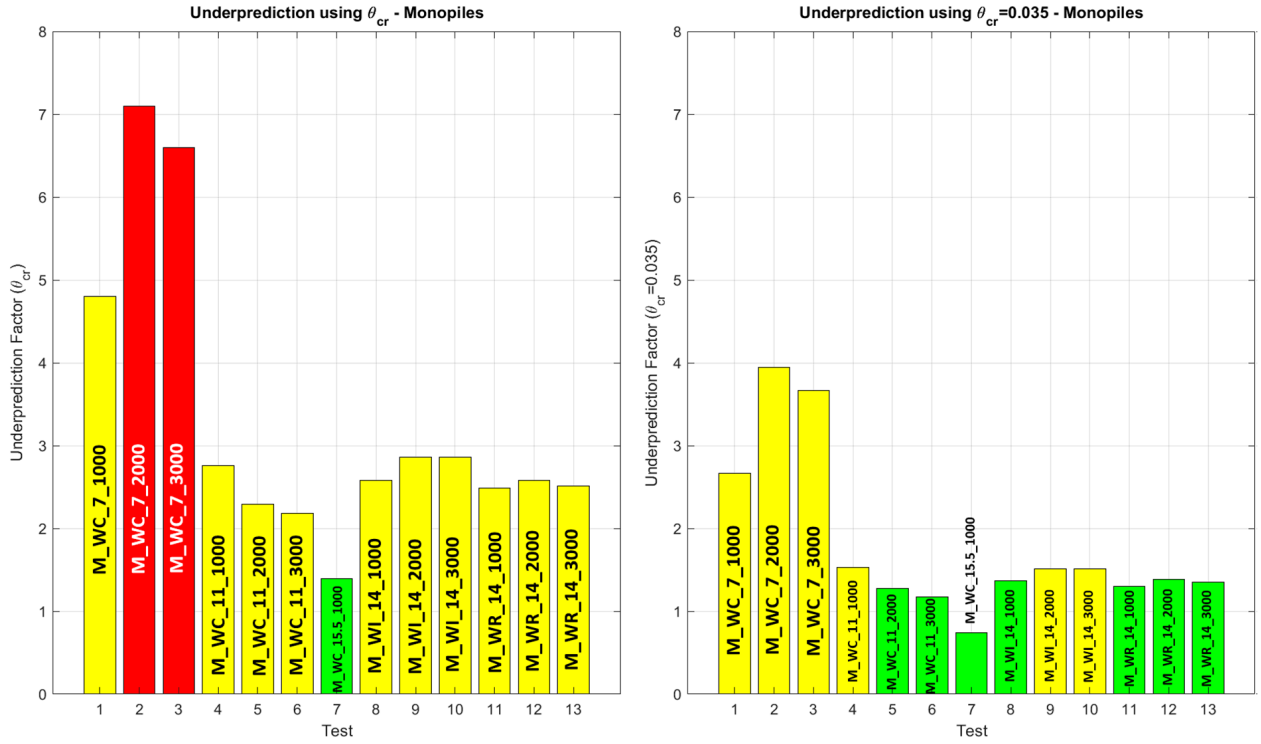


Figure 21. Underprediction factor for monopiles, using different values for the θ_{cr}—green: under 1.5 times; yellow: between 1.5 and 5 times; red: over 5 times.

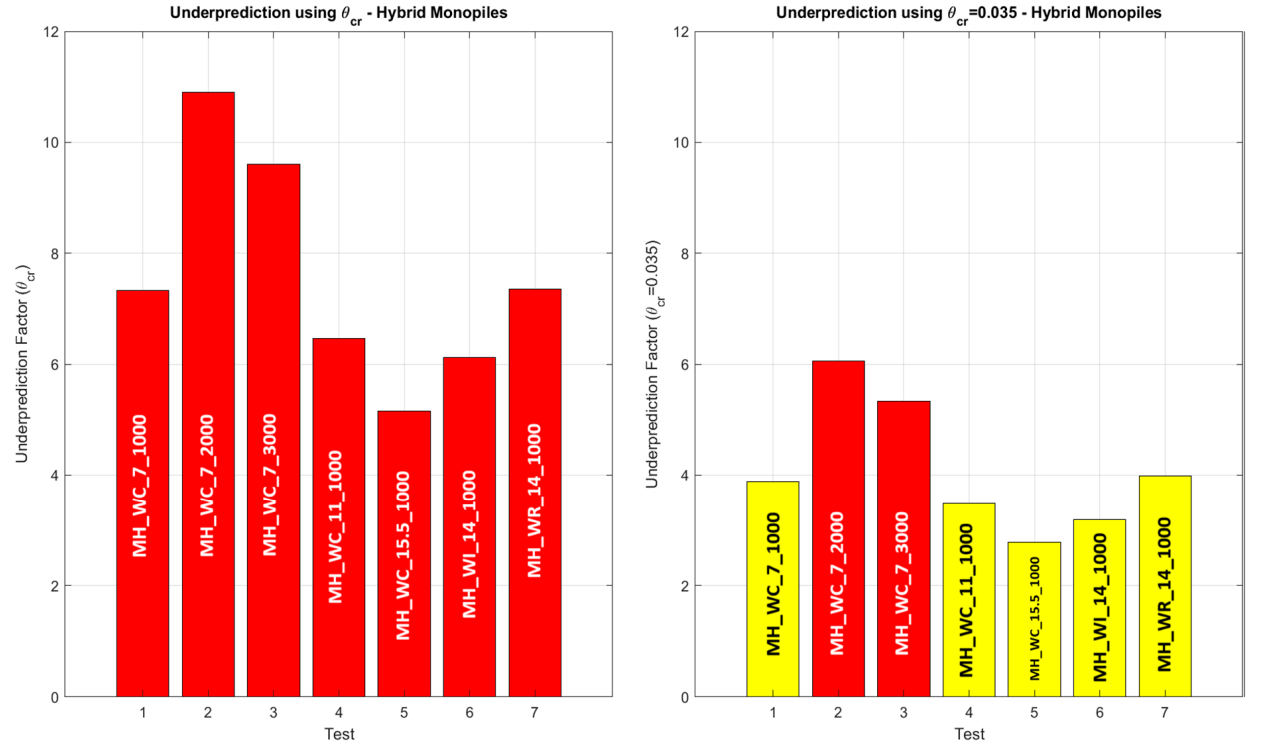


Figure 22. Underprediction factor for hybrid monopiles, using different values for the θcr—yellow: between 1.5 and 5 times; red: over 5 times.

Nonetheless, the discrepancy between the measured vs. predicted scour depths for the hybrid monopile, in comparison to the monopile foundation, underlines the limitations and insufficiencies that current predictive models have in capturing the complexity that hybrid structures and WEC components and oscillatory movement integration induce

in unsteady flow fields and offshore hydrodynamics. This reinforces the need for new predictive approaches tailored to multifunctional offshore structures that integrate in situ flow and seabed erosion measurements.

With the available metrics for assessing the scour protection condition, the parameter S/t_s (scour depth relative to the protection thickness) or the S_{3D}/n_s (scour damage relative to the number of armour layer rock units) emerges as a more reliable damage indicator and/or predictor than the S/D_p. Unlike the S/D_p ratio, which lacks a clear physical correlation with the specific characteristics of the scour protection's armour layer, such as D_{n50} or overall thickness, both S/t_s and S_{3D}/n_s directly reflect a direct and quantitative measure of the current state of the armour layer. For instance, a specific S/D_p value, even with known protection characteristics, offers limited insight into the protection's behaviour, failing to illustrate whether failure occurred or if the scour countermeasure is in a dynamic/static state. While it quantitatively distinguishes different erosion magnitudes, it provides only a generalised appreciation of damage without offering significant qualitative information regarding the protection status or comparable information regarding the protection's integrity. It provides greater utility in contexts where scour is measured without a scour protection, where the magnitude of the seabed erosion relative to the monopile offers a generalised sense of risk of ultimate and/or serviceability limit-state to the foundation. Conversely, S/t_s and S_{3D}/n_s directly and unambiguously translate the percentage of protection in the evaluated area that has been eroded, offering a clear and actionable understanding of its condition. Furthermore, for hybrid foundations, where enhanced flow patterns due to the paddles' movements and increased turbulence affect the erosion of the rubble-mound material, these parameters also offer sufficient credibility and a simpler visual representation and interpretation of the protection's behaviour.

Although the classification of scour protections into deformation classes with the evaluation of MOB_{top}-KC_{tot} is considered by [22] to be more useful than the standard behaviour classification (static, dynamic, and failure), it also acknowledges that the evaluation is not so straightforward and sometimes hard to determine. As shown in Figures 23 and 24, most of the tests fall within the range of several deformation classes. An attempt to assess a specific deformation class for each test was made considering the description provided by [22] and the photographic record made during the tests, plus the DTMs and S_{3D} distribution results in Figures A1–A20—see Table 8.

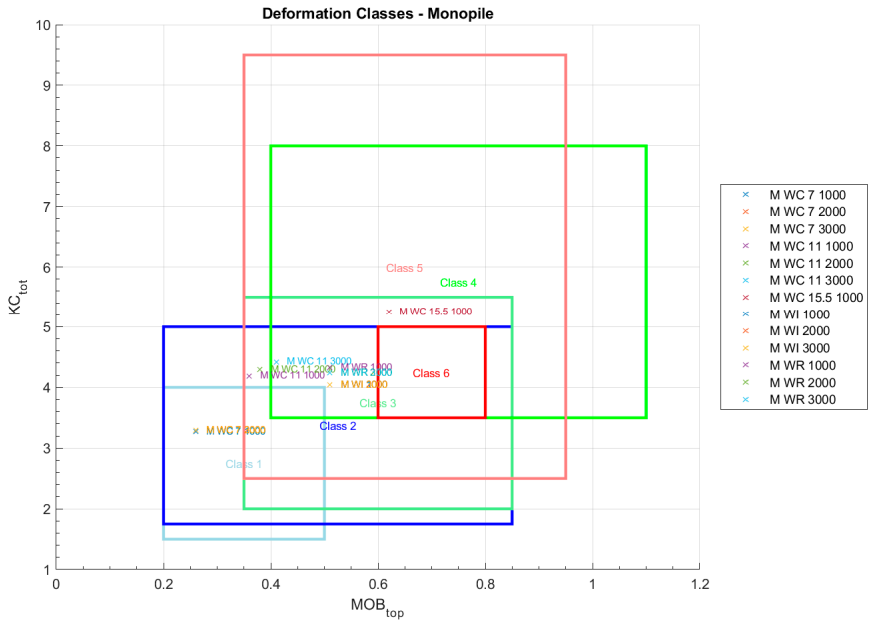


Figure 23. Deformation classes for monopile tests.

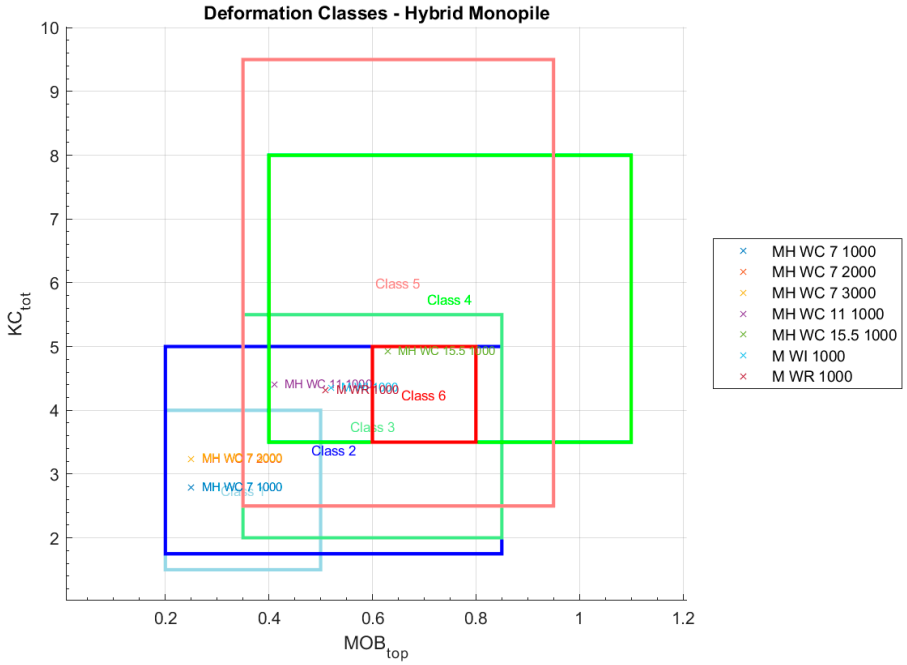


Figure 24. Deformation classes for hybrid monopile tests.

Table 8. Assessment of deformation class according to the criteria defined in [22].

Test #	Deformation Class Assessment	Possible Classes (Figures 23 and 24)
M_WC_7_1000	Class 1	Class 1 or 2
M_WC_7_2000	Class 1	
M_WC_7_3000	Class 1	
M_WC_11_1000	Class 1	Class 2, 3, or 5
M_WC_11_2000	Class 1	Class 2, 3, or 5
M_WC_11_3000	Class 3	Class 2–5
M_WC_15.5_1000	Class 2 (or 6)	Classes 3–5
M_WI_14_1000	Class 2 (or 6)	Classes 2–5
M_WI_14_2000	Class 2 (or 6)	
M_WI_14_3000	Class 2 (or 6)	
M_WR_14_1000	Class 2 (or 6)	Classes 2–5
M_WR_14_2000	Class 2 (or 6)	
M_WR_14_3000	Class 2 (or 6)	
MH_WC_7_1000	Class 1	Class 1 or 2
MH_WC_7_2000	Class 3	
MH_WC_7_3000	Class 3	
MH_WC_11_1000	Class 4+	Class 2–5
MH_WC_15.5_1000	Class 3+	Classes 2–6
MH_WI_14_1000	Class 6+	Classes 2–5
MH_WR_14_1000	Class 6+	Classes 2–5

Although the monopile tests were found to fall within one of the expected classes of deformation, a distinction was made in [22] based on whether the deformation occurred predominantly in the upstream or downstream area of the pile. When analysing the experimental tests in this study, it was observed that the damage occurred mainly within the vicinity of the pile, way inside the amplification area, mainly on the right and left sides.

Moreover, in some cases, the deformation pattern was not evident in the photographic registration. It was only perceptible using the DTMs and the S_{3D} results using the overlapping technique described in [21]. Additionally, according to the description of each class made by [22], the M_WC_15.5, M_WI, and M_WR tests should fall in class 6, since that class is associated with tests using low current velocities or cases with wave-only conditions. The tests M_WC_11_1000 and M_WC_11_2000 were classified as being in class 1, despite Figure 23 showing them outside of that class boundary. However, it was also reported in [22] that many tests expected to fall within a certain class may lie within the limits of other classes, or even outside of all defined class boundaries, due to significant overlaps.

Regarding the hybrid monopile tests, only the MH_WC_7 test sequence was in identifiable conditions to be placed within one of the described classes. For all the remaining tests, the scour damage was too excessive to identify a possible dominant location for the deformation in the protection or lack thereof. Therefore, considering the definition of each class presented in [22], each test was classified into the most appropriate class, considering the hydrodynamic conditions used in each test, and by adding a "+" sign in front of it, as a note of the extensive damage rates observed.

While categorising deformations by classes is deemed by [22] as a more useful classification, the fact is that it is not a linear, practical, or trivial task. From low to extreme scour deformations, distinguishing and classifying them could be challenging due to overlapping or even superposition of classes. Furthermore, it is possible to have deformation classes outside any boundary condition. This makes this classification system a highly subjective tool and less intuitive than the standard classification (static, dynamic, failure). However, directly comparing the MOB_{top} and KC_{tot} to the damage number proved noteworthy.

Overall, S_{3D} tends to increase with higher values of both variables (Figure 25), and regarding the monopile tests, it has a higher correlation with MOB_{top} number than the KC_{tot} parameter (weak correlation). Since MOB_{top} measures the hydraulic loading relative to the resistance of the armour layer, essentially reflecting the potential for erosion/movement of the armour layer units, it provides high-quality information about the scour protection resistance to the loads and whether it might fail. Therefore, it directly captures the actual effects of the main scour mechanisms on scour, resulting in a higher correlation with the damage number. On the other hand, despite KC_{tot} being a measure of the wave–current contribution relative to the structure, which is directly related to the shear stress amplification and vortex shedding around the monopile, primary causes of scour, in the end, it is a composite metric. Consequently, it may obscure the direct contribution of each hydrodynamic component to scour under varying flow conditions, as they may vary independently. Given that multiple wave–current regime combinations may yield identical KC_{tot} values, relying on this parameter may result in less accurate interpretations regarding the primary scour driver. This could explain the observed low correlation with the damage number.

As for the hybrid monopile tests, since severe scour deformations were observed, a high correlation between both KC_{tot} and MOB_{top} to S_{3D} was expected. The interaction between the WEC paddles and the flow leads to a highly energetic near-bed environment. The resulting scour deformation is influenced by intensified oscillatory flow patterns (captured by KC number) and increased hydraulic stress acting on the seabed protection (captured by MOB parameter). As a result, the high correlation with damage number was confirmed, indicating that scour is governed jointly by enhanced shear stresses and the armour layer's ability, or lack thereof, to resist them.

As the relation between the S_{3D} and the MOB_{top}-KC_{tot} model showed mixed results across the different structures, a more in-depth analysis was conducted. The analysis considers the influence of KC_{tot} (wave–current contribution), the KC number (wave contri-

bution), and the KC_c (current contribution). Additionally, an evaluation of the U_{cw} ratio in relation to the S_{3D} was also performed, since prior studies [31,34–38] have reported a general trend of increased scour depths for higher U_{cw} values under varying conditions. It is reported in the literature that for the same U_{cw} value, scour depths tend to increase for higher KC numbers [34]. That observation was considerably more pronounced in wave-dominant regimes. As U_{cw} increases, that correlation starts to weaken, and for $U_{cw} > 0.65$, scour depths remained almost constant and independent of KC number.

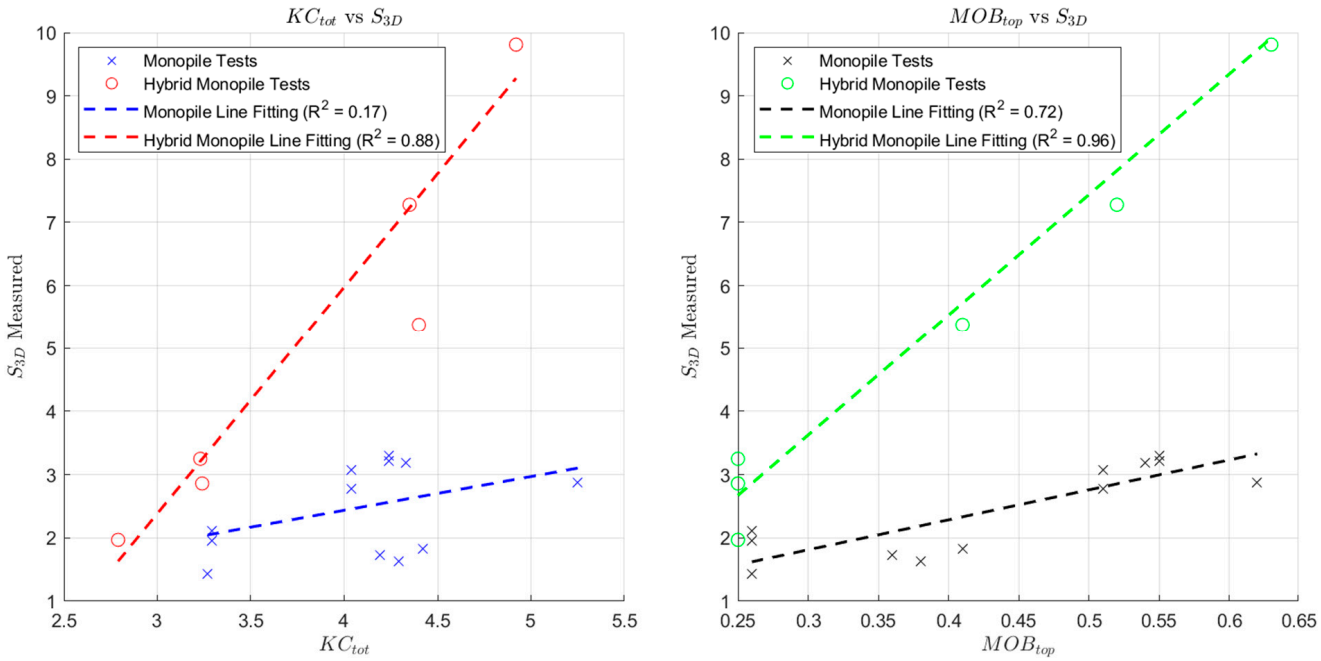


Figure 25. Damage number comparison with KC number (**left**) and MOB parameter (**right**).

As previously mentioned, although the KC_{tot} is directly associated with shear stress amplifications and scour, a clearer notion of the main scour drivers for each foundation emerges when its wave (KC) and current (KC_c) components are considered separately (Table 9). For the hybrid monopile, the results exhibit strong positive correlations between the KC_{tot} and KC, underscoring the predominant influence of wave-induced velocities enhanced by the WEC on the scour development (Figure 26). The moderate inverse correlation with the KC_c, Figure 27, indicates a comparatively lower influence of currents on scour for this type of structure. Conversely, for the monopiles, a strong positive correlation with the KC and a strong negative correlation with KC_c were identified—Figures 26 and 27. This observation supports the earlier assertion that the combined parameter may mask the distinct influences of each individual hydrodynamic component to scour, since for the same KC_{tot} value, multiple KC and KC_c combinations are possible. In the end, the strong correlation of damage with KC and KC_c, despite the weaker correlation observed with the KC_{tot}, is an indicator that monopile scour is highly dependent on the complex interaction between the two main hydrodynamic loads, which may not be fully encapsulated by a single combined parameter.

When interpreting the specific influence of the four parameters (KC_{tot}, KC, KC_c, and U_{cw}) on the damage number, any assessment should be made carefully. The apparent inverse correlation between the U_{cw} and S_{3D} (Figure 27) reflects the hydrodynamic conditions selected for the tests, in which higher S_{3D} values occurred for lower U_{cw} ratios as well as higher wave heights with lower current velocities (high KC and low KC_c). In contrast, lower scour damage rates were recorded for tests with higher U_{cw} ratios, which corresponded to lower wave heights and higher current velocities (low KC and high KC_c).

However, when analysing tests with comparable KC_{tot} values, e.g., M_WC_11 (U_{cw} = 0.55, $KC_{tot} \approx$ 4.2 to 4.4, KC ≈ 1.9 to 2.1) vs. M_WR_14 (U_{cw} = 0, KC_{tot} = KC ≈ 4.2 to 4.3), the test with the higher KC number (M_WR_14) presented almost a 60 to 90% increment on the S_{3D} value. Furthermore, when comparing the wave-only tests (M_WI vs. M_WR), both with the same U_{cw} value, the test series with a higher KC number presented slightly higher scour damage, as reported by [34]. As for the tests with higher U_{cw} ratios, the ones with smaller KC numbers presented similar S_{3D} values for the monopile tests, slightly higher for the H_s = 0.07 m and U_{cw} = 0.65 combination versus the H_s = 0.11 m and U_{cw} = 0.55 one—consistent with the observations reported by [31,34–38].

Table 9. $S_{3D,measured}$, U_{cw}, KC, KC_c, and KC_{tot} comparison.

Test	U_{cw}	KC	KC_c	KC_{Tot}	$S_{3D,measured}$
M_WC_7_1000	0.65	1.17	2.10	3.27	1.43
M_WC_7_2000	0.65	1.19	2.10	3.29	2.11
M_WC_7_3000	0.64	1.19	2.10	3.29	1.95
M_WC_11_1000	0.55	1.90	2.29	4.19	1.73
M_WC_11_2000	0.55	1.98	2.31	4.29	1.63
M_WC_11_3000	0.53	2.12	2.30	4.42	1.83
M_WC_15.5_1000	0.18	4.34	0.91	5.25	2.87
M_WI_14_1000	0.00	4.04	0.00	4.04	2.77
M_WI_14_2000		4.04	0.00	4.04	3.08
M_WI_14_3000		4.04	0.00	4.04	3.08
M_WR_14_1000	0.00	4.33	0.00	4.33	3.18
M_WR_14_2000		4.24	0.00	4.24	3.30
M_WR_14_3000		4.24	0.00	4.24	3.21
MH_WC_7_1000	0.67	0.95	1.84	2.79	1.97
MH_WC_7_2000	0.65	1.15	2.08	3.23	3.25
MH_WC_7_3000	0.65	1.14	2.10	3.24	2.86
MH_WC_11_1000	0.53	2.10	2.30	4.40	5.38
MH_WC_15.5_1000	0.19	4.01	0.91	4.92	9.81
MH_WI_14_1000	0.00	4.35	0.00	4.35	7.28
MH_WR_14_1000	0.00	4.31	0.00	4.31	8.55

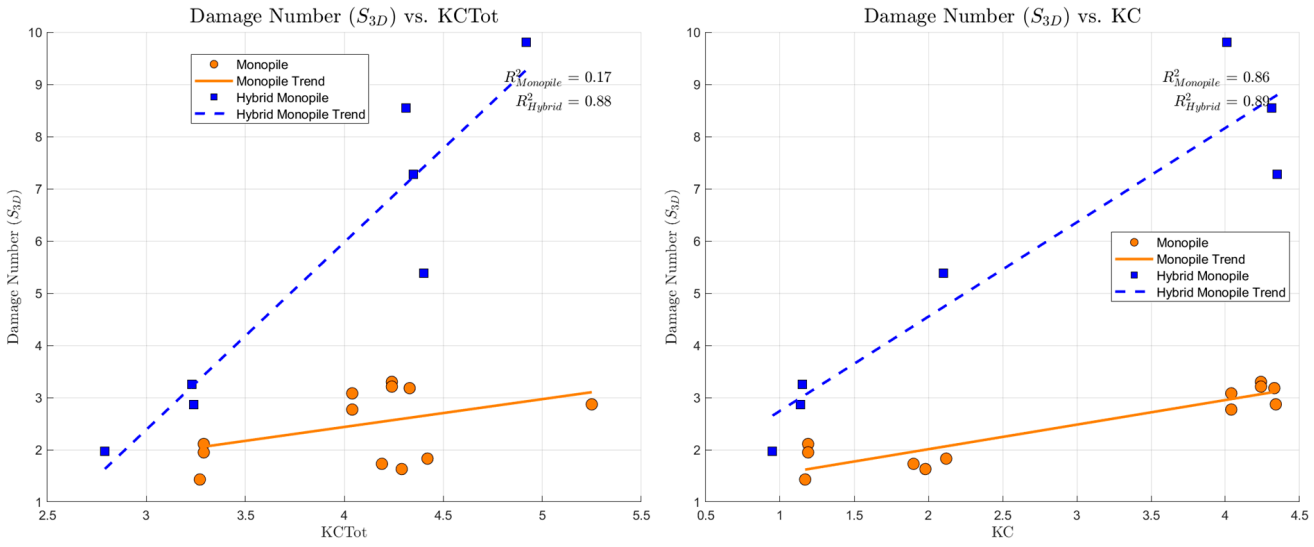


Figure 26. S_{3D} analysis for the KC_{tot} and KC number.

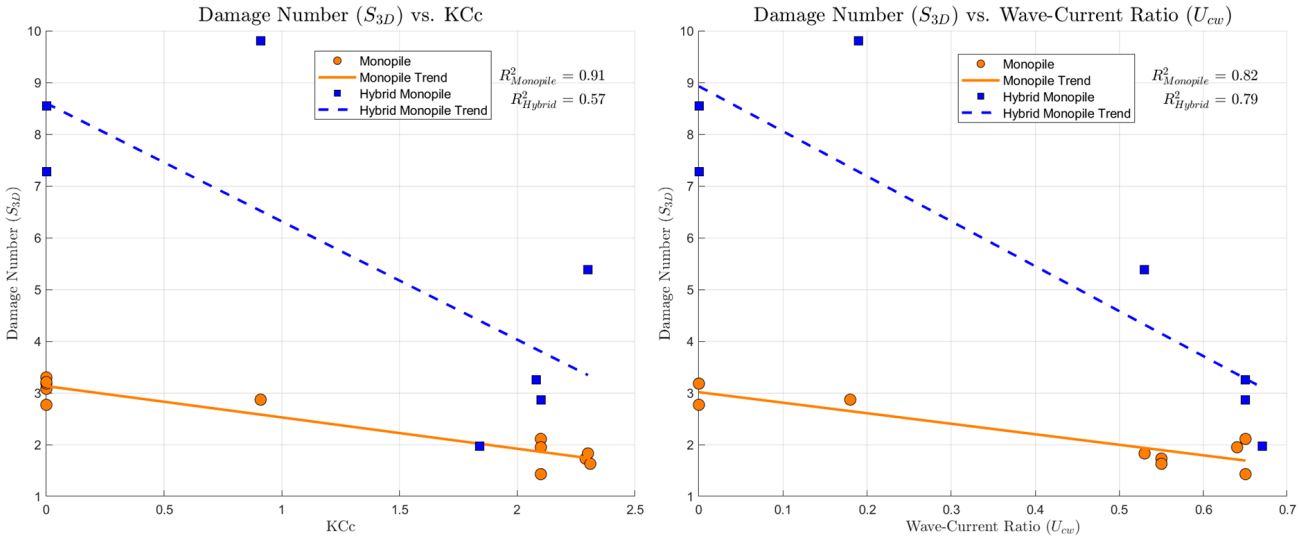


Figure 27. S_{3D} Analysis for the KC_c and the U_{cw} ratio.

Overall, the results point to the fact that scour damage increases with increasing KC values, regardless of the prevailing regime.

When comparing the monopile test results with the hybrid monopile, it is evident that the influence previously observed for lower U_{cw} ratios was more pronounced for the hybrid monopile tests. That difference can be attributed to the unique hydrodynamic interactions generated by the oscillating paddle movement of the OSWEC. In wave-dominated regimes, that oscillatory motion induces substantial variations in the local flow velocities and conditions. These interactions enhance bed shear stresses, turbulence, and flow accelerations around the structure, acting as a supplementary source of scour-inducing force, thus promoting increased sediment transport when compared to conventional monopile foundations under similar conditions.

3.4. Wave Transmission (C_{Tr}) and Wave Reduction (C_{Red}) Coefficients

The main goal of the experimental campaign was to assess damage to the scour protection of two different types of foundations. However, converting a standard monopile into a hybrid structure by incorporating a WEC revealed significant flow patterns and hydrodynamic differences. Since the focus was not on the performance of the WEC, the captured energy efficiency or the power per unit front was not calculated. Instead, straightforward metrics such as the wave transmission coefficient (C_{Tr}), which compares the seaside wave height to the leeside wave height in each test, and the wave reduction coefficient (C_{Red}), which compares the wave heights between a monopile test and a hybrid monopile test for the same hydrodynamic condition, highlight how both foundations, including the device, influence wave attenuation.

For monopile-only tests, the C_{Tr} consistently remains near 100% (Table 10), indicating minimal interference with the incoming wave. The structure's narrow cross-section contributes to this behaviour, allowing waves to propagate with negligible attenuation, reaffirming the limited wave sheltering capacity—deviations in the coefficient do not exceed ±5%. In contrast, for hybrid monopiles, the integrated WEC allows a significant reduction in the C_{Tr}, especially for higher wave heights, where almost 25% of wave reduction on the leeside was observed. These results were achieved using a simplified mechanical system to actuate the WEC paddles, suggesting that a fully functional PTO system could achieve even greater attenuation. The results support the premise that hybridisation effectively increases the dissipative capacity, enhancing wave absorption and reducing transmitted wave energy. On the other hand, as a negative impact, it increases the flow contraction and

the wave–current velocities (not quantified in this study) between the WEC's bottom and the scour protection.

Table 10. Wave transmission coefficients (C_{Tr}).

Test	Number of Waves	C_{Tr} (%)
M_WC_7_1000	1000	100.0
M_WC_7_2000	1000	100.0
M_WC_7_3000	1000	100.0
M_WC_11_1000	1000	105.0
M_WC_11_2000	1000	104.8
M_WC_11_3000	1000	102.7
M_WC_15.5_1000	1000	98.7
M_WI_14_1000	1000	99.3
M_WI_14_2000	1000	97.8
M_WI_14_3000	1000	96.3
M_WR_14_1000	1000	101.4
M_WR_14_2000	1000	102.1
M_WR_14_3000	1000	100.0
MH_WC_7_1000	1000	94.6
MH_WC_7_2000	1000	94.4
MH_WC_7_3000	1000	94.3
MH_WC_11_1000	1000	81.8
MH_WC_15.5_1000	1000	76.8
MH_WI_14_1000	1000	75.4
MH_WR_14_1000	1000	86.1

While some seaside C_{Red} values (Table 11) for the hybrid monopile show slight negative values, i.e., wave enhancement up to 9%, this was attributed to the intense scour that eroded out the protection and caused the lowering of the seabed, which increased the water depth, creating conditions for bigger waves to be registered without breaking. The leeside C_{Red} values (Table 11) consistently reflect the substantial wave height reduction across all the hybrid tests, up to almost 30%. These results highlight the potential of WECs as promising components for integration into offshore structures. They may serve not only as a booster for renewable energy and power generation but also as a protective element that shields offshore structures and mitigates the effects of severe coastal erosion [8,9]. Nevertheless, the optimisation and strategic integration of PTO systems appear critical for addressing the scour enhancement associated with such devices. This phenomenon could otherwise undermine the overall efficiency of the hybrid structure.

Table 11. Wave reduction coefficients (C_{Red}).

Test	Number of Waves	Seaside C_{Red} (%)	Seaside C_{Red} (%)
M_WC_7 vs. MH_WC_7	1000	−2.7	2.9
	1000	2.8	9.0
	1000	4.3	10.6
M_WC_11 vs. MH_WC_11	1000	−9.1	16.7
M_WC_15.5 vs. MH_WC_15.5	1000	−0.6	27.5
M_WI_14 vs. MH_WI_14	1000	−1.4	29.8
M_WR_14 vs. MH_WR_14	1000	3.6	22.0

Despite the presence of the WEC, a reduction in transmitted wave height was observed compared to the incident wave. However, the scour damage to the protection was concurrently enhanced. This suggests that the rotational angle of the converter's paddle and its distance to the seabed must be considered a critical design criterion to mitigate excessive scour or damage in the protection. When using an OSWEC as a protective measure for a pipeline, it was concluded by [39] that scour was reduced by increasing the angle between the flap and the seabed, which translated to a reduction in the flap's rotation relative to its vertical axis, thereby minimising its oscillatory movement and velocity.

Regarding the distance of a converter to the seabed, the influence of the tip clearance (defined as the vertical distance between a rotating blade and a stationary point) for tidal-current energy turbines was investigated by [40,41], with [40] specifically studying turbines attached to a monopile. Both studies demonstrated that scour was increased by the converter due to enhanced local velocities, downflow, and the occurrence of horseshoe vortices. A 10–20% increase in scour extent and a 30% increase in the scour depth were reported by [41]. Furthermore, it was observed that scour increased faster with lower distances to the bed profile. Nonetheless, it was also concluded that equilibrium scour is independent of tip clearance—a continuous decrease in the distance to the sediment bed, after a certain point, did not translate to a significant increase in the scour depth [41].

While this study maintained a fixed tip clearance, based on operational recommendations for the WEC, it is important to highlight that this parameter significantly influences scour development and could be critical to the future of hybrid foundations. Upcoming studies should consider a range of tip clearance distances and their interaction with other variables associated with the WEC and foundation geometry to quantify their impact under various hydrodynamic conditions. This would allow for a more comprehensive understanding of its influence on scour and ultimately support the development of tailored design criteria for scour protection of hybrid foundations incorporating WEC devices.

4. Conclusions

Experimental results revealed that, despite the WECS's ability to attenuate incident hydrodynamic conditions, reducing leeward wave heights up to almost 30%, the oscillatory motion of the convergent paddles induced complex flow patterns. These patterns, which include downflow, horseshoe vortices, and lee–wake vortices, intensified scour mechanisms and led to severe scour on the armour layer unit, including the erosion and lowering of the seabed near the structure.

Applying the overlapping-circle methodology [21] to determine S_{3D} number proved effective and precise in quantifying the damage rate, allowing for a detailed characterisation of its distribution. The analysis of the influence of the grid ratio ($\eta_{S3D,grid}$) on the quantification of $S_{3D,max}$ showed a strong dependency of this parameter on the selected circle sub-area size (A_{sub}), reinforcing the need for a uniform failure criterion. The results suggest that a grid ratio between 1/6 and 1/4, corresponding to sub-areas of $6D_{n50}^2$ and $4D_{n50}^2$, may be suitable for evaluating the damage number, validating, to some extent, the failure criterion suggested by [12] as a reasonable limit. However, the measured damage values raise significant questions about the applicability and conservatism of existing design criteria and formula [7].

The comparison between the monopile and hybrid monopile tests demonstrated a clear difference in the scour rate and the damage number (S_{3D}). Riprap protections on hybrid foundations suffered significantly higher damage, resulting in pronounced deformations and, in many cases, premature failure (often within the first 1000 waves), unlike monopiles, which, under mild conditions, maintained integrity or exhibited dynamic behaviour. Although some protection configurations showed some capacity for reshaping

and recovery, even after significant damage, in the case of the hybrid monopile, the intensity of the flow patterns induced by the WEC led to irreversible damage to the armour layer. These findings suggest that existing design criteria, particularly those developed for monopiles [7], are insufficient to comply with more complex and hybrid configurations. It can be argued that evaluating the S/t_s or S_{3D}/n_s ratio emerges as a more reliable and representative damage indicator for riprap scour protections than the S/D_p ratio or $S_{3D} > 1.0$ failure limit suggested by [7]. The proposed limits for S/t_s or S_{3D}/n_s align better with the experimentally observed behaviour of the scour protections.

The scour prediction formula developed by [22], which relies on MOB_{top} and KC_{tot} parameters, was found to consistently underestimate the scour deformation observed during the tests, mainly for the hybrid foundation ones. This discrepancy may be related to this study's small dataset, differences in model scales, or even differences in the subareas of each measurement methodology. Hence, the methodology proposed by [22] also proved unsuitable for accommodating the increased complexity introduced by a WEC in a hybrid foundation system. However, a strong correlation was established between S_{3D} and KC_{tot} number, as naturally, the scour damage has a higher relation to the shear stress amplification and vortex shedding around the monopile. Moreover, although [22] reported no clear dependency on some parameters, such as gradation width, thickness, and extent, future studies could benefit from assessing the contribution of some of these parameters as they could exert a measurable influence on scour under combined wave–current and WEC-induced loading. Ideally, bridging the S_{3D} with the MOB_{top}-KC_{tot} model could be extremely valuable for developing a more robust approach to damage prediction for both monopiles and hybrid foundations.

This research also contributes to a deeper understanding of hydrodynamic interactions in hybrid offshore foundations, underlining the need to revise existing scour protection design frameworks. While based on a small dataset, the results point towards new design criteria, with guidelines that should incorporate structural complexities and dynamic load interactions to account for a broader spectrum of offshore and marine harvesting technologies, recognising the complexity introduced by hybrid structures and WEC motion.

In summary, the novel contributions and main takeaways are hereby highlighted:

- **Application of a scour protection in a hybrid monopile-WEC system:** comparative assessment of scour damage with a monopile foundation.
    - **Paddle-based WECs can intensify scour in hybrid foundations:** although the used OSWEC device attenuated incoming wave heights by almost 30%, its oscillatory movement generates complex flow patterns and significantly increases the scour damage.
- **Application and evaluation of the innovative overlapping-circle 3D method:** demonstration of its effectiveness and high-resolution scour quantification capabilities of the method proposed by [21], while comparing it with two other different methods [7,22], making a sensitivity analysis to understand the need for a methodological standardisation.
    - **Overlapping method revealed limitations in existing design damage analysis methods:** the overlapping method effectively quantified scour damage via S_{3D} number, providing more insights into its behaviour, completing the information acquired from the studies performed by [7,22], mainly for hybrid configurations. However, its high sensitivity to the grid ratio indicates that the optimal value should fall within the 1/4 and 1/6 ratio interval, which aligns with the proposal made by [21].

- **Identification of limitations in existing design standards and predictive formulas:** the results lead to questioning the conservatism of existing design standards and their inability to capture WEC-induced enhanced flow complexities.
    - **Hybrid monopile riprap protections exhibited early failure:** when compared to standard monopile tests, the scour countermeasures applied to hybrid structures showed markedly higher damage rates, often failing within the initial 1000 waves, thus indicating that the current design methods do not accommodate the dynamic loads induced by WECs.
- **Proposal of alternative performance-aligned scour metrics:** S/t_s and/or S_{3D}/n_s ratios offer more accurate and straightforward indicators for quantifying and evaluating riprap scour protection performance in complex offshore environments by shifting the comparative/relative referential from the foundation to the protection itself.
    - **Alternative S/t_s and S_{3D}/n_s indicators shown to be reliable:** these two relative scour damage ratios better represent the actual riprap state and performance under hydrodynamic loading than the traditional S/D_p or $S_{3D} > 1.0$ threshold, offering a more reliable basis for future design approaches.
- **Framework for advancing design methodologies in hybrid offshore foundations:** to update predictive tools that account for dynamic structural effects and vortex-induced shear amplifications of coupling (extra) devices, to promote safer, more adaptable infrastructures for marine harvesting technologies.

Future research should prioritise expanding the experimental test matrix to include a broader range of hydrodynamic scenarios, alternative scour protection configurations, and different WEC devices. It also should address secondary erosion behind riprap protections since it may become significant under long-term operational conditions. While the present study focused on the performance of scour protection under a maximum of 3000 waves, aligned with most tests reported in the literature and consistent with the duration used to develop the current design criteria, it represents a step toward understanding the short- to mid-term behaviour of such protective systems. Subsequent studies should aim to complement this research through extended physical/numerical modelling campaigns (e.g., over 5000 waves) and field observations to assess potential long-term damage mechanisms, including secondary erosion. Moreover, the recoverability capacity, an indicator of dynamic stability, registered during the tests should also be evaluated for long-term durations as well, to determine whether the backfilling reflects a sustainable resilience or merely a temporary delay of failure. Comparative tests using different types of filter layers would be valuable to observe if the phenomenon persists across different configurations or if it may be a signal of progressive failure. Such efforts would help validate whether existing design standards sufficiently tackle these longer-term effects.

The use of a simplified spring-based mechanism over a PTO in the present research allowed for a controlled assessment of the first-order influence of WEC paddle motion on scour. To more accurately determine the direct influence of the converter, future tests should incorporate a fully operational PTO system to consider the damping effects, as it is expected to significantly affect the flap dynamics, alter the flow patterns, and ultimately influence the scour damage around the foundation. Furthermore, a direct quantification of the local flow enhancement induced by the hybrid structure should be assessed via a CFD model. Such a model would enable the determination of the influence of the converter's paddle motion on the resulting pressure field variations, quantify the enhancement in the bed shear stress acting on the armour layer, and delineate the relative contribution of each flow pattern to the scour damage measured on the scour protection.

Addressing these knowledge gaps will enable the expansion of the existing datasets and raise the current understanding of the key physical mechanisms driving scour in WECs and hybrid systems. This is essential for advancing the comprehension of scour damage processes and ultimately to develop a robust predictive framework. Such efforts are critical to improve or propose new design methodologies and formulations that would be capable of accurately capturing the complex interactions in these intricate marine and offshore environments.

Author Contributions: Writing—original draft preparation, formal analysis, visualisation, J.C.; conceptualisation, J.C., T.F.-F. and P.L.; methodology, J.C., T.F.-F. and M.W.; writing—review and editing, J.C., T.F.-F., M.W., F.T.-P. and P.L.; supervision, T.F.-F., F.T.-P. and P.L.; funding, T.F.-F.; project administration, T.F.-F. and F.T.-P. All authors have read and agreed to the published version of the manuscript.

Funding: J. Chambel acknowledges funding in the form of a Ph.D. scholarship grant awarded to J. Chambel by the Portuguese Foundation for Science and Technology (FCT) and the European Social Fund (ESF) of the European Union (EU), with the reference number 2021.07393.BD (https://doi.org/10.54499/2021.07393.BD). This work was performed in the scope of the POSEIDON project (Project Reference: PTDC-ECI-EGC-5177-2020), which was funded through the FCT.

Data Availability Statement: The data that support the findings of this study are available from the corresponding author, J.C., upon reasonable request.

Acknowledgments: The authors would like to acknowledge Miguel Guerra for the support and expertise during the physical modelling experiments.

Conflicts of Interest: The authors declare no conflicts of interest.

Abbreviations

The following abbreviations are used in this manuscript:

ADV	Acoustic Doppler Velocimeter
$A_{failure}$	Area of failure
A_{sub}	Area of the overlapping-circle sub-areas
a_0, a_2, a_3	Regression fitting coefficients
a_1, a_4	Coefficient for hydrodynamic conditions
b_0	Regression fitting coefficient
C_{Red}	Wave reduction coefficient
C_{Tr}	Wave transmission coefficient
D	Scour protection's armour layer extent
D^*	Dimensionless grain size
D_{cr}	Critical stone size
D_p	Pile diameter
D_{n50}	Nominal stone diameter of the scour protection
D_{15}	15th percentile of scour protection material grading
D_{50}	Mean stone diameter of the scour protection material
$D_{67.5}$	67.5th percentile of scour protection material grading
D_{85}	85th percentile of scour protection material grading
DTM	Digital Terrain Model
D	Water depth
d_{16}	16th percentile of sediments
d_{50}	Mean diameter of sediments
d_{84}	84th percentile of sediments
F_r	Froude number
FOSWEC	Floating Oscillating Surge Wave Energy Converter
GBF	Gravity-based Foundation

g	Gravitational acceleration
H	Wave height
H_{m0}	Spectral significant wave height
H_s	Significant wave height
KC	Keulegan–Carpenter number (wave contribution)
KC_c	Keulegan–Carpenter number (current contribution)
KC_{tot}	Total Keulegan–Carpenter number (wave–current contribution)
MOB	Mobility parameter
MOB_{top}	Mobility parameter on the top layer of scour protection
N	Number of waves
n_s	Number of rock stone sizes (layers)
OSWEC	Oscillating Surge Wave Energy Converter
OWT	Offshore Wind Turbine
p	Multiplication factor for overlapping-circle sub-area
R_{circle}	Radius of overlapping-circle sub-area
R_e	Reynolds number
S	Scour depth
$S_{predicted}$	Predicted scour depth
S/D_p	Relative scour depth
S/t_s	Scour depth relative to the scour protection thickness
$S_{predicted}/D_p$	Predicted relative scour depth
S_{3D}	Damage number
$S_{3D,failure}$	Damage number for failure limit
$S_{3D,max}$	Damage number (maximum)
$S_{3D,measured}$	Damage number (measured)
$S_{3D,predicted}$	Damage number (predicted)
$S_{3Dsub,circle}$	Damage number for overlapping-circle sub-area
S_{3D}/n_s	Damage number relative to the number of rock stone sizes (layers)
s	Specific density (ρ_s/ρ_w)
stab	Stability parameter
T	Wave period
T^*	Dimensionless time scale
T_m	Mean wave period
$T_{m-1,0}$	Energy wave period
T_p	Wave peak period
TEC	Tidal-current Energy Converter
t_s	Scour protection thickness
U_c	Depth-averaged current velocity
U_{cr}	Mean threshold velocity of sediments
U_{cw}	Wave–current velocity ratio
U_m	Wave orbital bottom velocity
$U_{m,top}$	Wave orbital bottom velocity at the top of the armour layer
$V_{A,max}$	Maximum erosion volume
V_{circle}	Volume of overlapping-circle sub-area
V_e	Eroded volume
WEC	Wave Energy Converter
w_s	Settling velocity
α	Amplification factor
$\Delta S_{3D}/n_s$	Damage increase ratio
$\eta_{S3D,grid}$	Grid ratio
θ	Shields parameter
θ_{cr}	Critical Shields parameter
θ_{max}	Maximum dimensionless wave–current-induced shear stress

ν	Kinematic viscosity of water
ρ_s	Density of rock material
ρ_w	Water mass density
σ_s	Standard deviation of sediments
τ_{cr}	Critical bed shear stress
τ_m	Mean combined bed shear stress (current and wave-induced)
τ_{max}	Maximum combined bed shear stress (current and wave-induced)
Y	Wave spectrum peak enhancement factor

Appendix A

Monopile and Hybrid Foundation S_{3D} Results: Overlapping Technique Results ($A_{sub} = 4D_{n50}^2$)

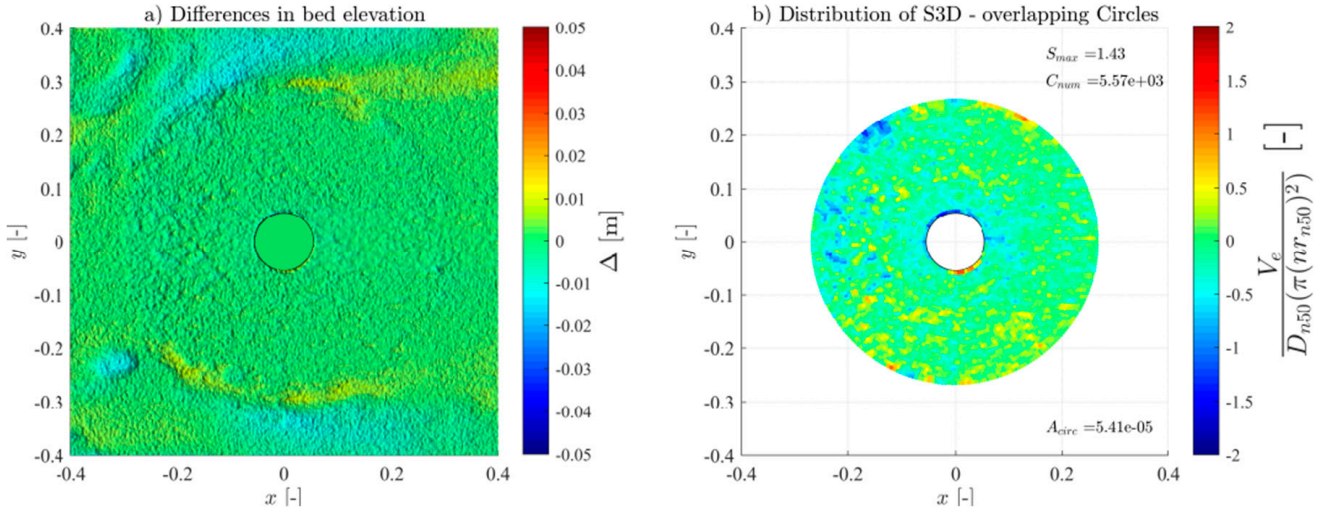


Figure A1. M_WC_7_1000 test: (**a**) DTM and (**b**) S_{3D} distribution—waves and currents from left to right.

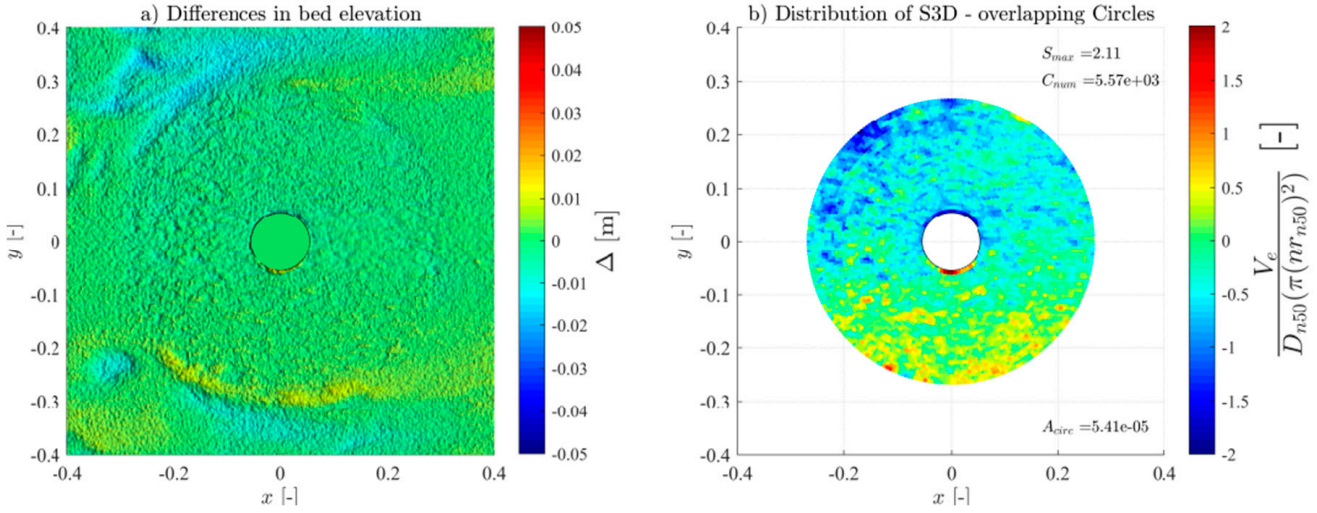


Figure A2. M_WC_7_2000: (**a**) DTM and (**b**) S_{3D} distribution—waves and currents from left to right.

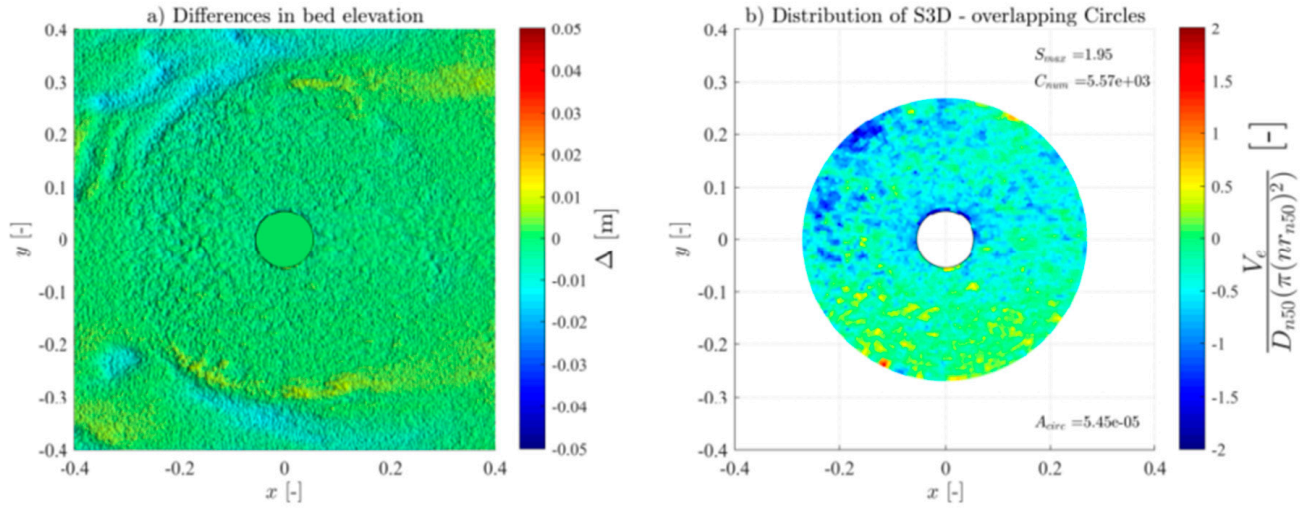


Figure A3. M_WC_7_3000 test: (**a**) DTM and (**b**) S_{3D} distribution—waves and currents from left to right.

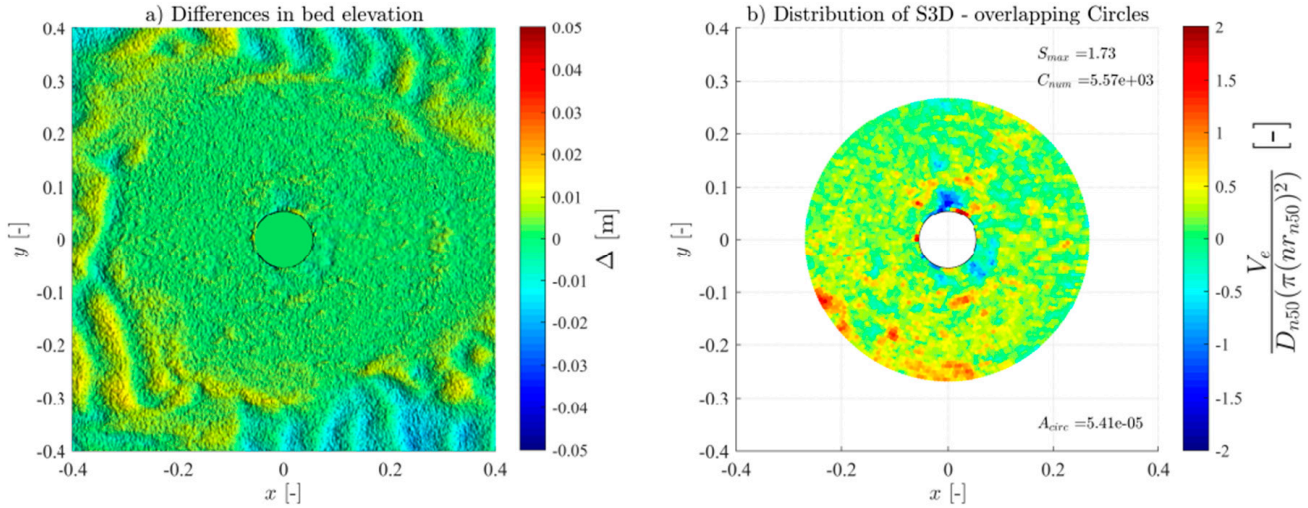


Figure A4. M_WC_11_1000 test: (**a**) DTM and (**b**) S_{3D} distribution—waves and currents from left to right.

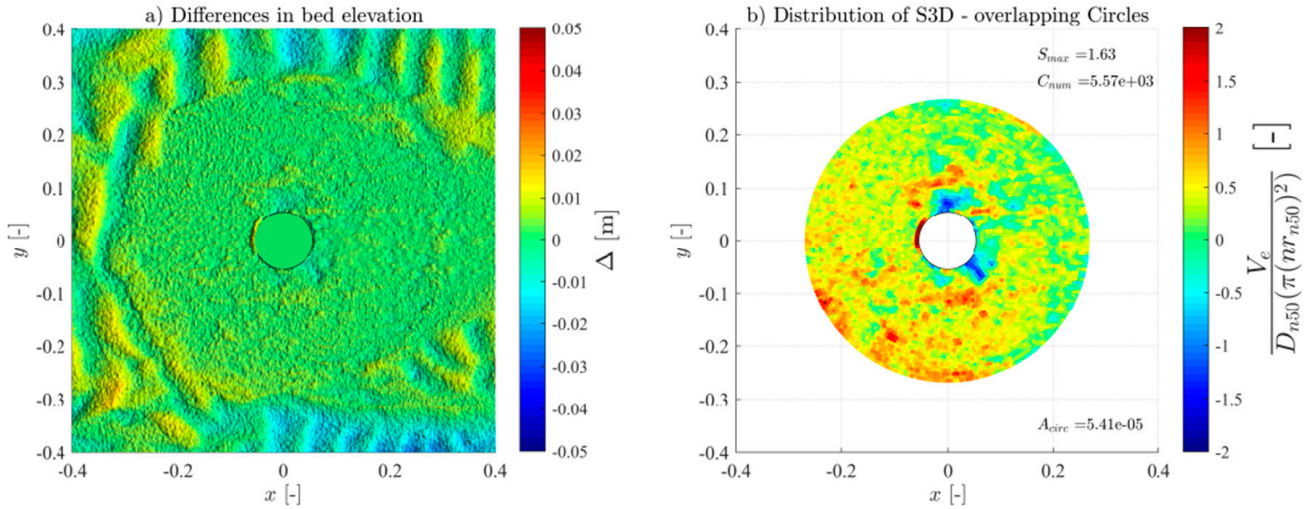


Figure A5. M_WC_11_2000 test: (**a**) DTM and (**b**) S_{3D} distribution—waves and currents from left to right.

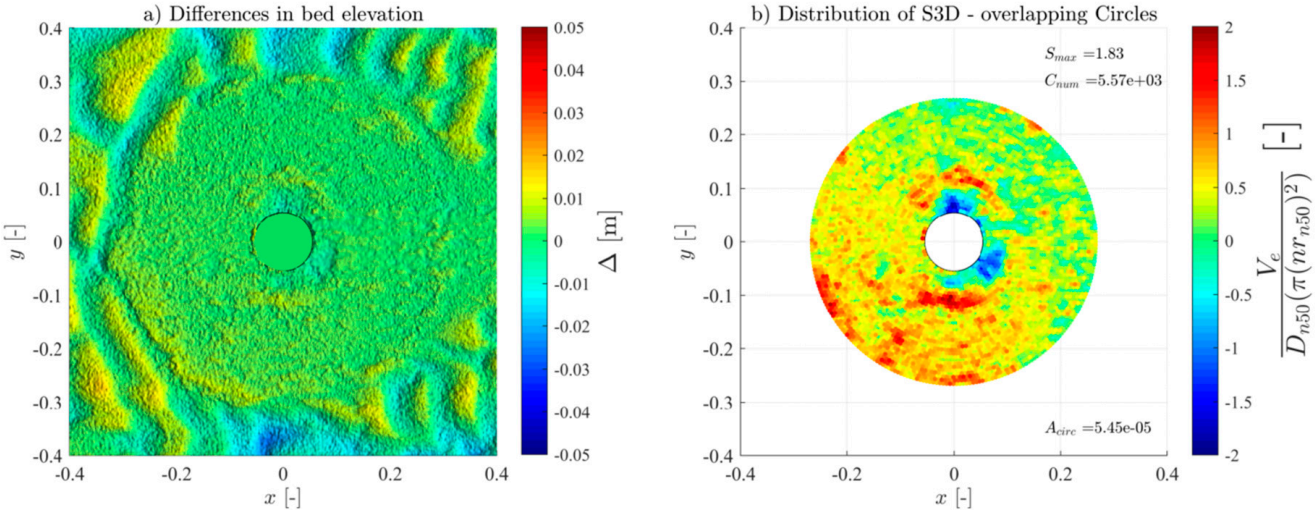


Figure A6. M_WC_11_3000 test: (**a**) DTM and (**b**) S_{3D} distribution—waves and currents from left to right.

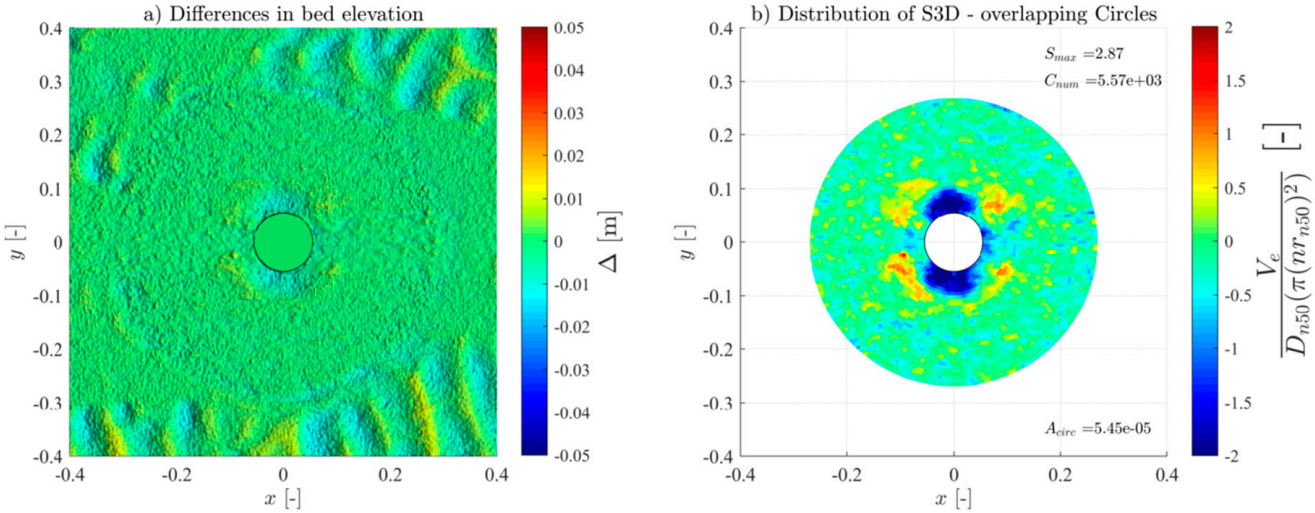


Figure A7. M_WC_15.5_1000 test: (**a**) DTM and (**b**) S_{3D} distribution—waves and currents from left to right.

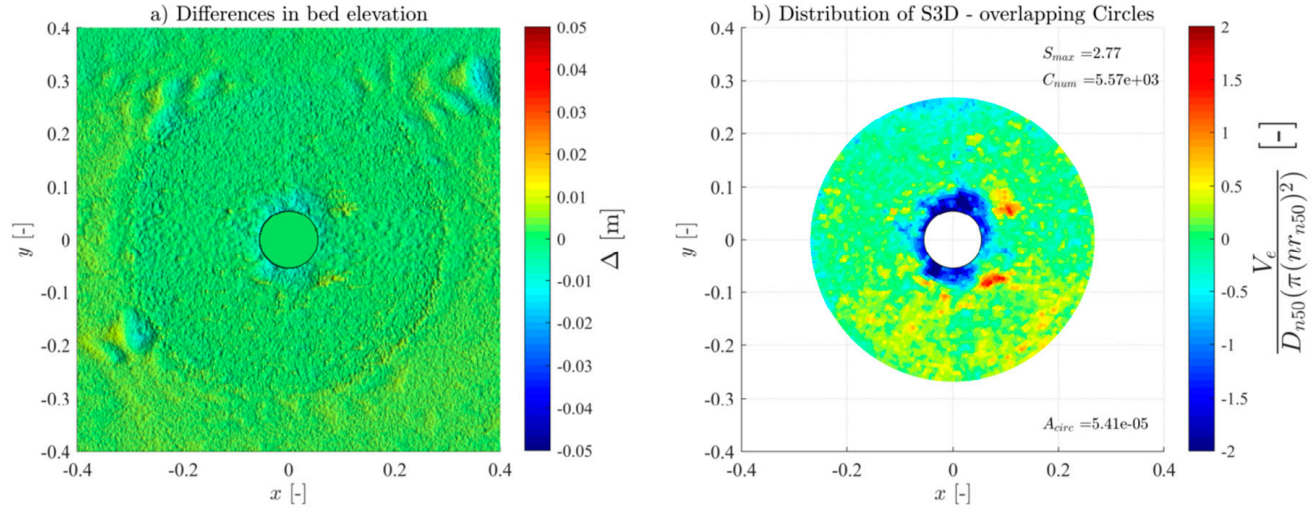


Figure A8. M_WI_14_1000 test: (**a**) DTM and (**b**) S_{3D} distribution—waves from left to right.

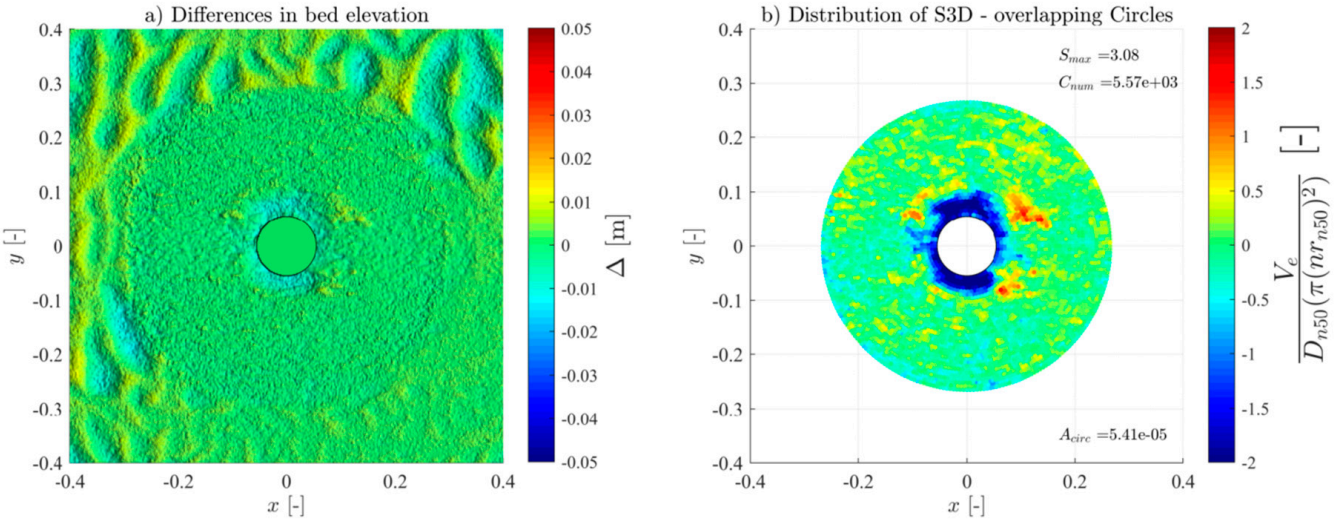


Figure A9. M_WI_14_2000: (**a**) DTM and (**b**) S_{3D} distribution—waves from left to right.

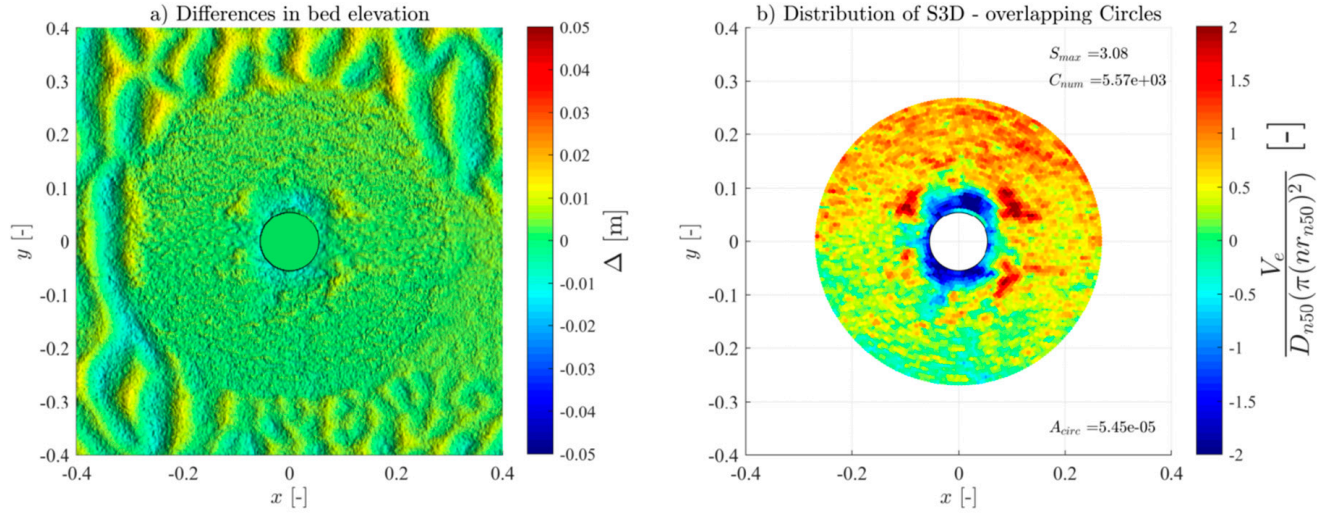


Figure A10. M_WI_14_3000 test: (**a**) DTM and (**b**) S_{3D} distribution—waves from left to right.

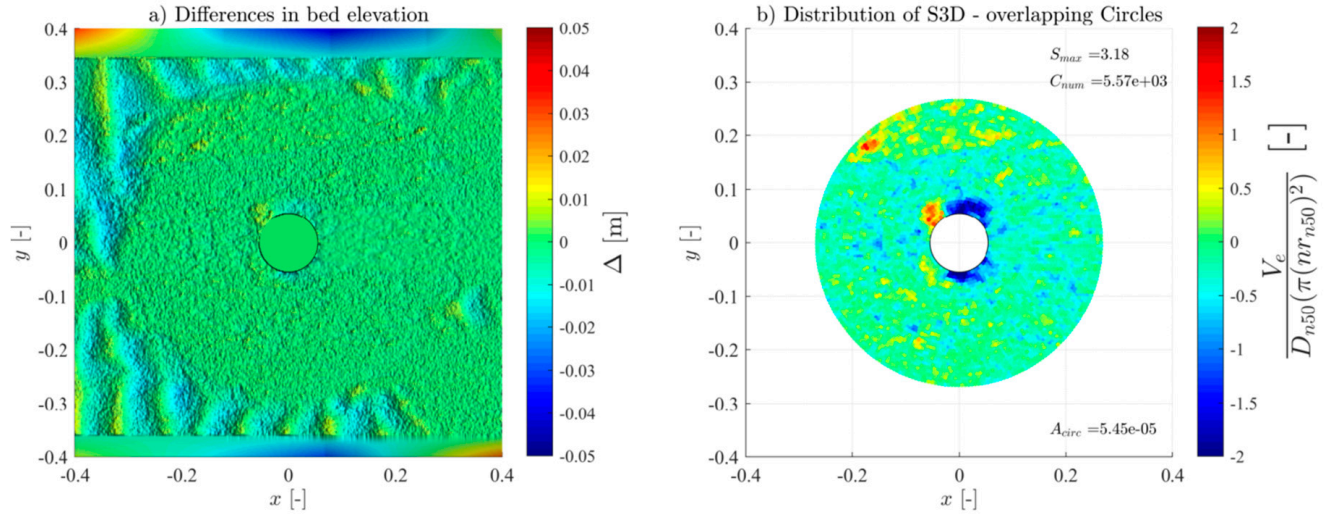


Figure A11. M_WR_14_1000 test: (**a**) DTM and (**b**) S_{3D} Distribution—waves from left to right.

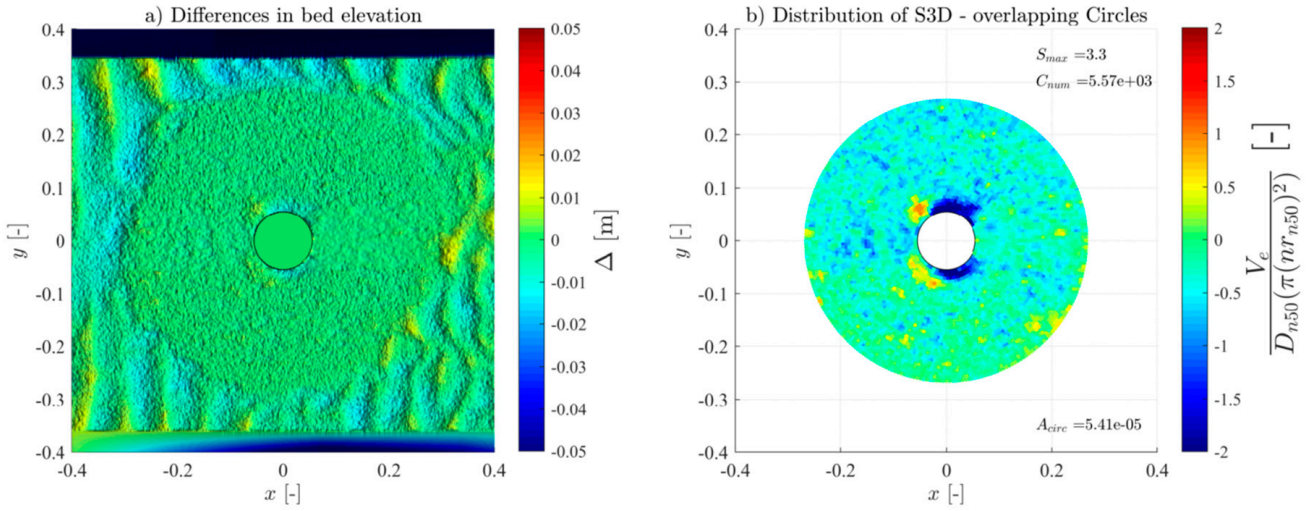


Figure A12. M_WR_14_2000 test: (**a**) DTM and (**b**) S_{3D} distribution—waves from left to right.

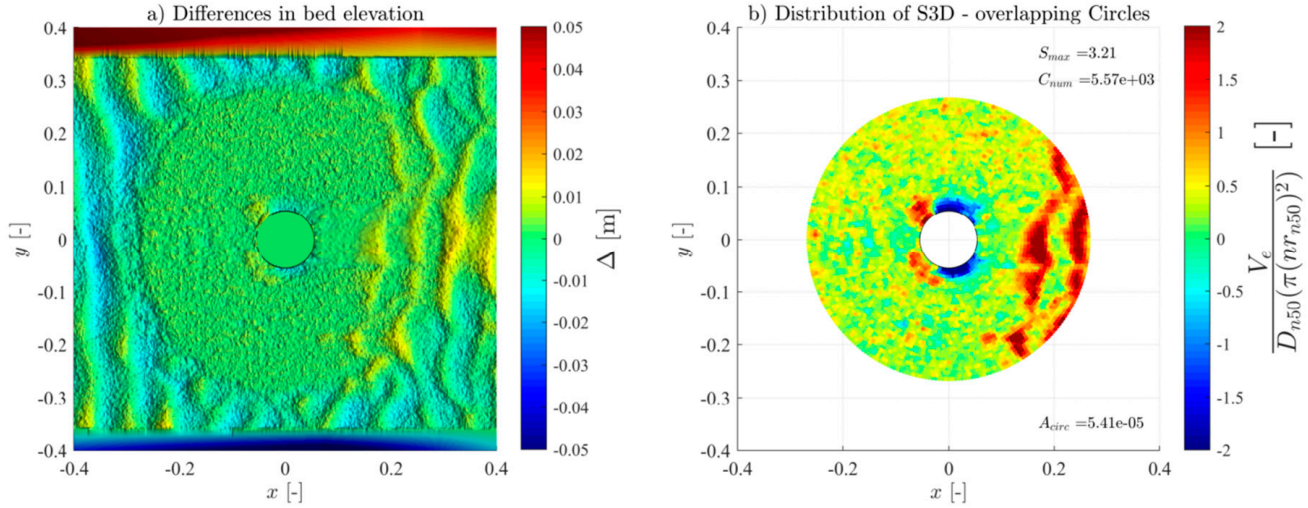


Figure A13. M_WR_14_3000 test: (**a**) DTM and (**b**) S_{3D} distribution—waves from left to right.

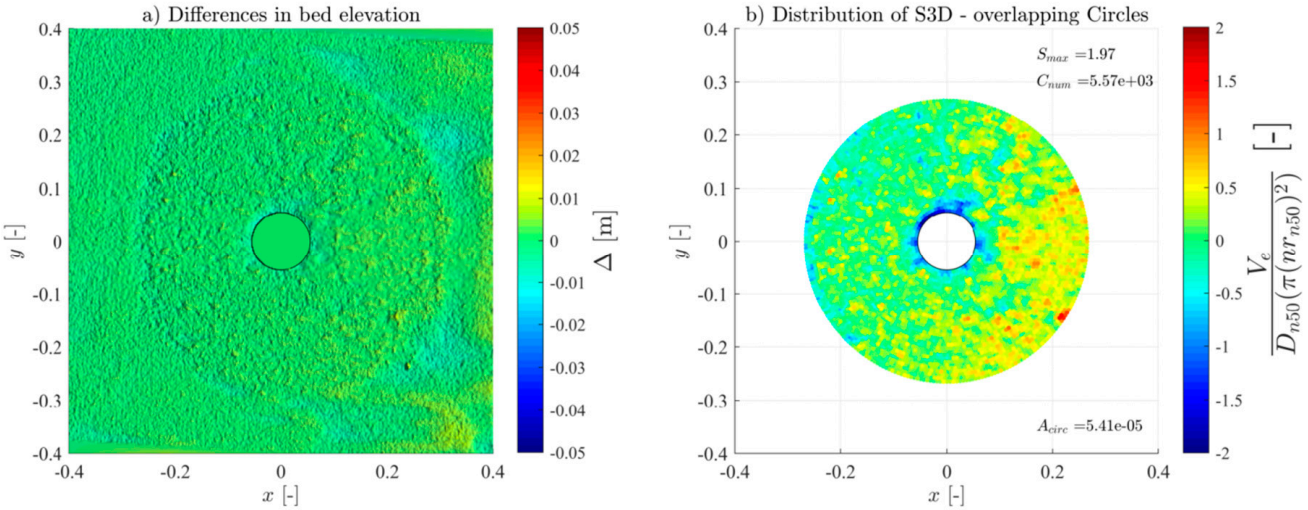


Figure A14. MH_WC_7_1000 test: (**a**) DTM and (**b**) S_{3D} distribution—waves and currents from left to right.

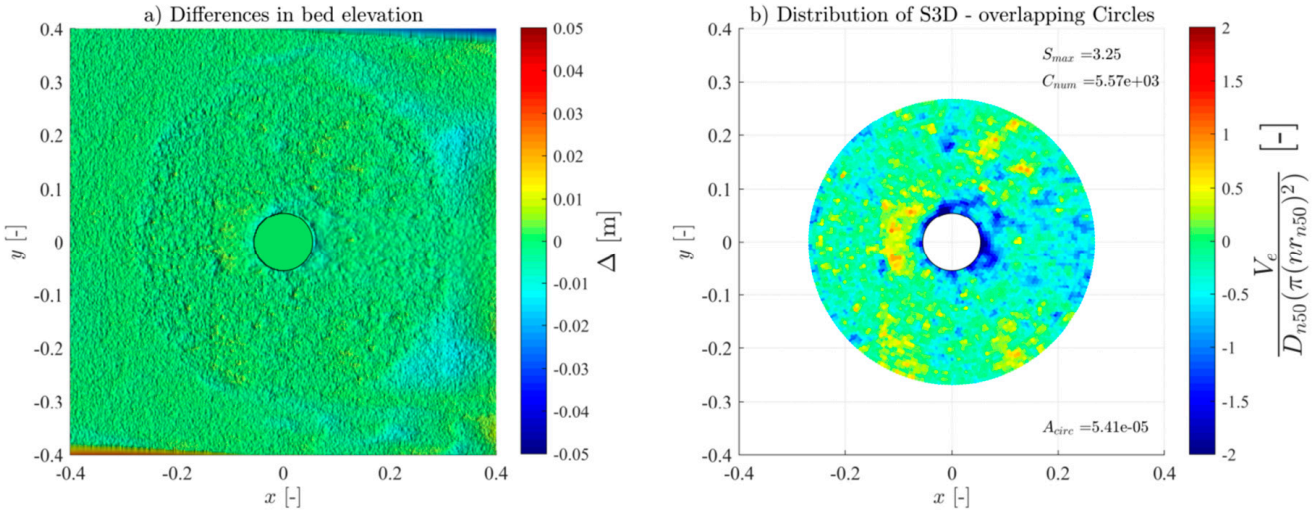


Figure A15. MH_WC_7_2000 test: (**a**) DTM and (**b**) S_{3D} distribution—waves and currents from left to right.

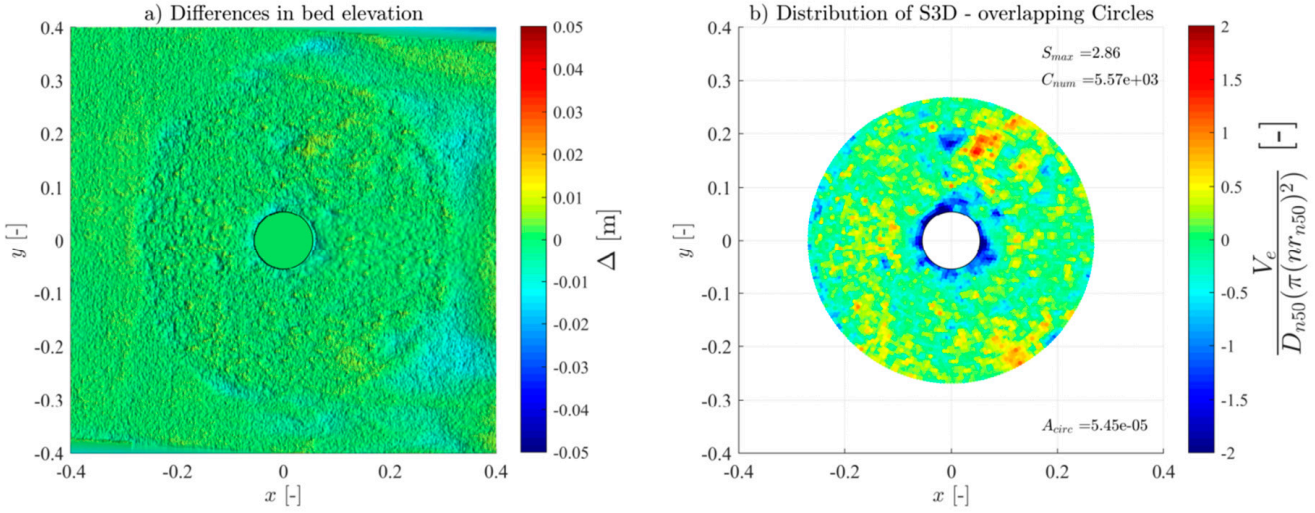


Figure A16. MH_WC_7_3000 test: (**a**) DTM and (**b**) S_{3D} distribution—waves and currents from left to right.

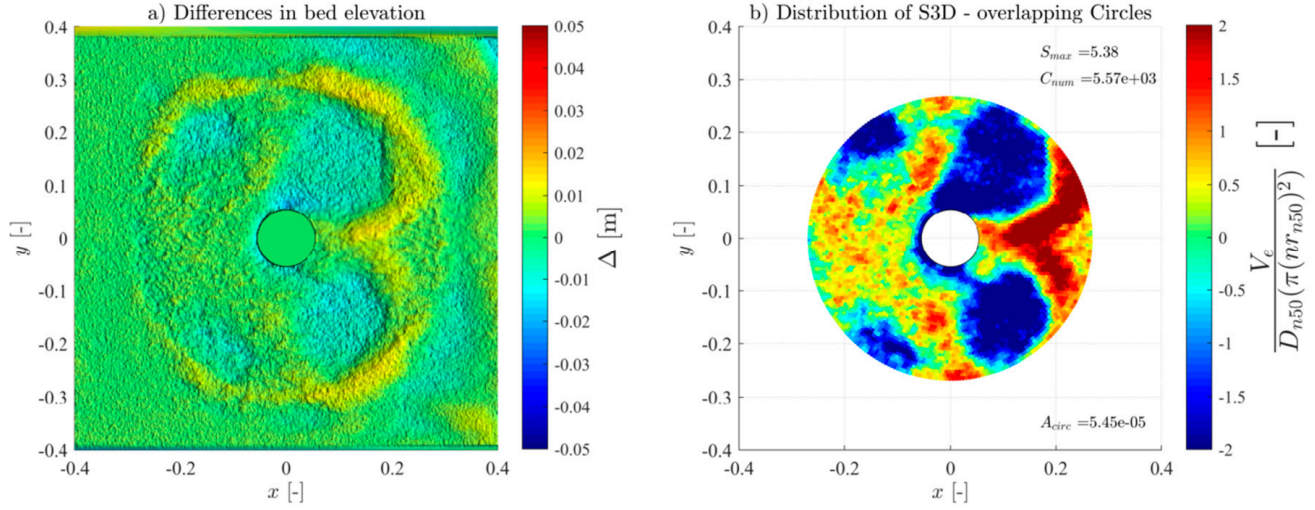


Figure A17. MH_WC_11_1000 test: (**a**) DTM and (**b**) S_{3D} distribution—waves and currents from left to right.

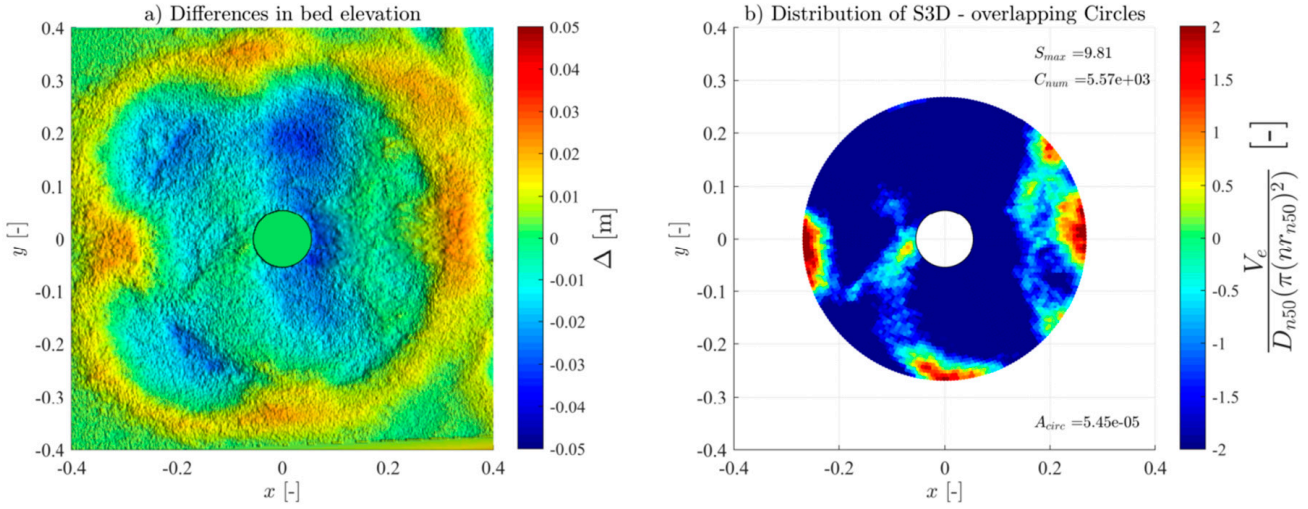


Figure A18. MH_WC_15.5_1000 test: (**a**) DTM and (**b**) S_{3D} distribution—waves and currents from left to right.

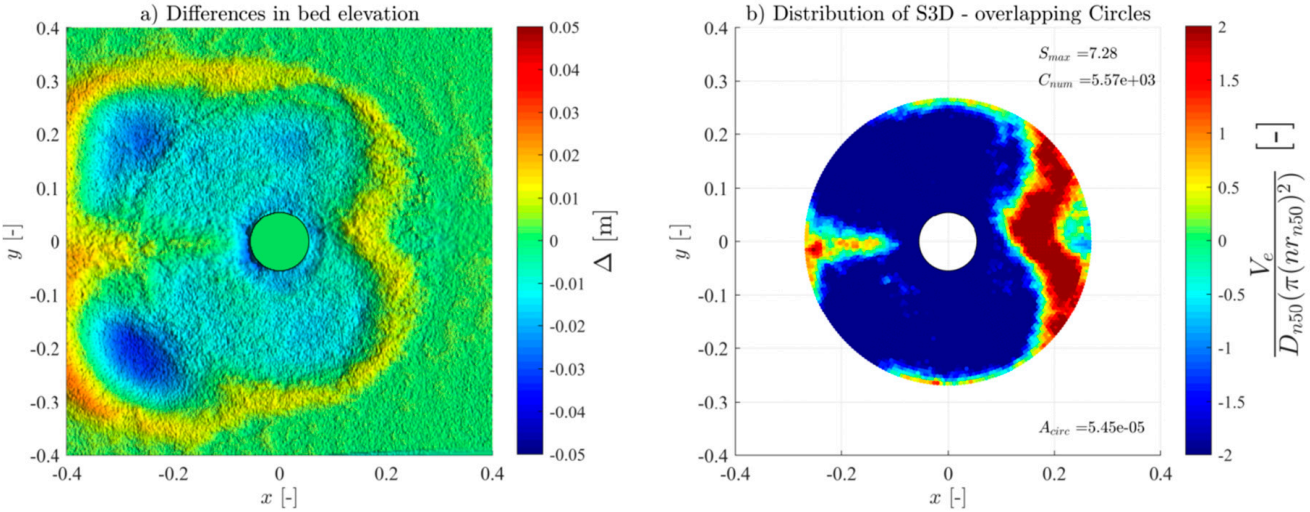


Figure A19. MH_WI_14_1000 test: (**a**) DTM and (**b**) S_{3D} distribution—waves from left to right.

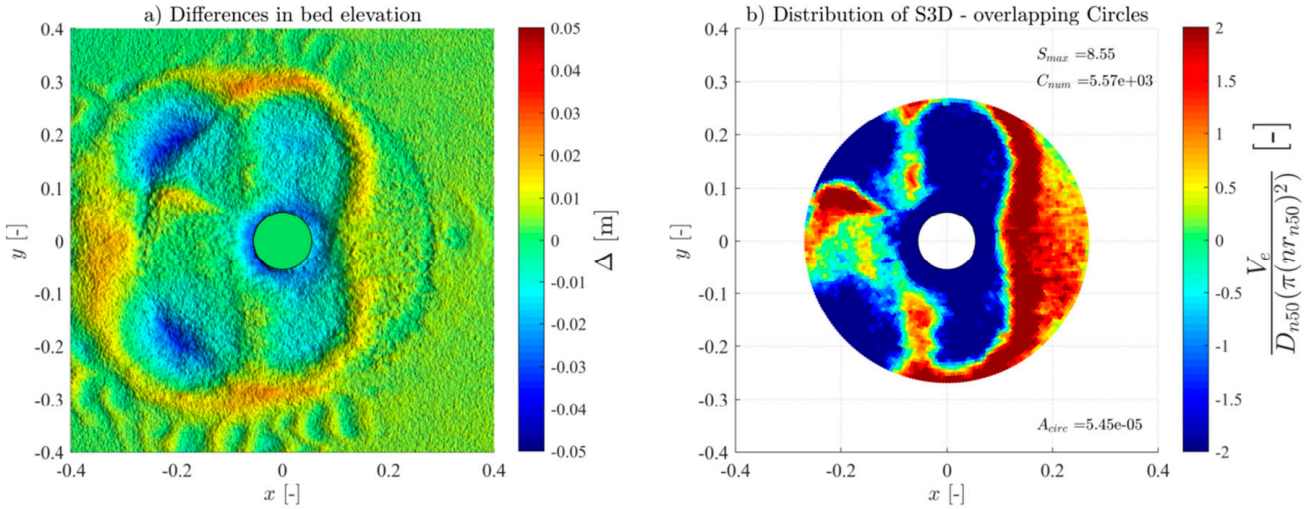


Figure A20. MH_WR_14_1000 test: (**a**) DTM and (**b**) S_{3D} distribution—waves from left to right.

Appendix B

Monopile and Hybrid Foundation S3D Results for Different Grid Ratios

Table A1. $S_{3D,measured}$ computation for different grid ratios—(A): M_WC_7_3000; (B): M_WC_11_3000; (C): M_WC_15.5_1000; (D): M_WI_3000; (E): M_WR_1000.

Monopile Tests						(A)	(B)	(C)	(D)	(E)
A_{sub}	Value [m^2]	$\eta_{S3D,grid}$	p Value	R_{circle} [m]	C_{num}	$S_{3D,measured}$				
D_{n50}^2	1.362×10^{-5}	1.000	1.1284	2.082×10^{-3}	23,200	3.46	2.71	3.96	3.42	5.26
$1.111D_{n50}^2$	1.513×10^{-5}	0.900	1.1894	2.194×10^{-3}	20,700	3.12	2.21	3.71	3.39	4.75
$1.5D_{n50}^2$	2.042×10^{-5}	0.667	1.3820	2.550×10^{-3}	15,400	3.03	2.49	3.71	3.36	4.77
$2D_{n50}^2$	2.723×10^{-5}	0.500	1.5958	2.944×10^{-3}	11,500	2.29	2.02	3.26	3.29	4.03
$3D_{n50}^2$	4.085×10^{-5}	0.333	1.9544	3.606×10^{-3}	7640	2.21	1.95	3.38	3.28	3.43
$4D_{n50}^2$	5.446×10^{-5}	0.250	2.2568	4.164×10^{-3}	5570	1.95	1.83	2.87	3.08	3.18
$5D_{n50}^2$	6.808×10^{-5}	0.200	2.5231	4.655×10^{-3}	4600	2.20	1.89	2.86	2.84	3.20
$6D_{n50}^2$	8.170×10^{-5}	0.167	2.7640	5.099×10^{-3}	3770	1.90	1.96	2.85	2.67	2.95
$7D_{n50}^2$	9.531×10^{-5}	0.143	2.9854	5.508×10^{-3}	3250	1.94	1.78	2.79	2.63	2.59
$8D_{n50}^2$	1.089×10^{-4}	0.125	3.1915	5.888×10^{-3}	2780	1.76	1.87	2.93	2.82	2.71
$9D_{n50}^2$	1.225×10^{-4}	0.111	3.3851	6.246×10^{-3}	2550	1.91	1.85	2.78	2.85	2.82
$10D_{n50}^2$	1.362×10^{-4}	0.100	3.5682	6.583×10^{-3}	2150	1.70	1.64	2.69	2.70	2.49
$16D_{n50}^2$	2.179×10^{-4}	0.063	4.5135	8.327×10^{-3}	1400	1.75	1.61	2.68	2.55	2.30
$20D_{n50}^2$	2.723×10^{-4}	0.050	5.0463	9.310×10^{-2}	1100	1.58	1.51	2.58	2.55	2.30
$25D_{n50}^2$	3.404×10^{-4}	0.040	5.6419	1.041×10^{-2}	839	1.36	1.56	2.64	2.50	1.91
$50D_{n50}^2$	6.808×10^{-4}	0.020	7.9788	1.472×10^{-2}	409	1.24	1.34	2.40	2.07	1.69
$100D_{n50}^2$	1.362×10^{-3}	0.010	11.2838	2.082×10^{-2}	189	1.04	1.03	2.03	1.95	1.43
A_{pile}	9.503×10^{-4}	0.00143	29.8103	5.500×10^{-2}	24	0.62	−0.02	0.52	0.31	0.60

Table A2. $S_{3D,measured}$ computation for different grid ratios—(A): MH_WC_7_3000; (B): MH_WC_11_1000; (C): MH_WC_15.5_1000; (D): MH_WI_1000; (E): MH_WR_1000.

Hybrid Monopile Tests						(A)	(B)	(C)	(D)	(E)
A_{sub}	Value [m^2]	$\eta_{S3D,grid}$	p Value	R_{circle} [m]	C_{num}	$S_{3D,measured}$				
D_{n50}^2	1.362×10^{-5}	1.000	1.1284	2.082×10^{-3}	23,200	3.22	5.88	10.7	8.79	12.1
$1.111D_{n50}^2$	1.513×10^{-5}	0.900	1.1894	2.194×10^{-3}	20,700	3.54	5.72	11.2	9.4	10.4
$1.5D_{n50}^2$	2.042×10^{-5}	0.667	1.3820	2.550×10^{-3}	15,400	3.31	5.97	11.4	8.64	10.9
$2D_{n50}^2$	2.723×10^{-5}	0.500	1.5958	2.944×10^{-3}	11,500	3.14	5.28	11.1	8.74	10.3
$3D_{n50}^2$	4.085×10^{-5}	0.333	1.9544	3.606×10^{-3}	7640	3.11	5.44	10.1	8.30	9.40
$4D_{n50}^2$	5.446×10^{-5}	0.250	2.2568	4.164×10^{-3}	5570	2.86	5.38	9.81	7.28	8.55
$5D_{n50}^2$	6.808×10^{-5}	0.200	2.5231	4.655×10^{-3}	4600	2.60	4.97	10.1	7.34	9.59
$6D_{n50}^2$	8.170×10^{-5}	0.167	2.7640	5.099×10^{-3}	3770	2.63	5.02	9.13	6.90	8.35
$7D_{n50}^2$	9.531×10^{-5}	0.143	2.9854	5.508×10^{-3}	3250	2.60	4.80	8.88	7.11	8.49
$8D_{n50}^2$	1.089×10^{-4}	0.125	3.1915	5.888×10^{-3}	2780	2.68	4.68	9.12	7.00	8.04
$9D_{n50}^2$	1.225×10^{-4}	0.111	3.3851	6.246×10^{-3}	2550	2.49	4.87	8.96	6.79	8.57

Table A2. *Cont.*

Hybrid Monopile Tests						(A)	(B)	(C)	(D)	(E)
A_{sub}	Value [m^2]	$\eta_{S3D,grid}$	p Value	R_{circle} [m]	C_{num}	$S_{3D,measured}$				
$10D_{n50}^2$	1.362×10^{-4}	0.100	3.5682	6.583×10^{-3}	2150	2.32	5.03	8.97	6.59	8.21
$16D_{n50}^2$	2.179×10^{-4}	0.063	4.5135	8.327×10^{-3}	1400	2.16	4.95	8.68	6.38	7.75
$20D_{n50}^2$	2.723×10^{-4}	0.050	5.0463	9.310×10^{-3}	1100	1.93	4.71	8.54	6.43	7.15
$25D_{n50}^2$	3.404×10^{-4}	0.040	5.6419	1.041×10^{-2}	839	1.95	4.39	8.41	6.38	7.48
$50D_{n50}^2$	6.808×10^{-4}	0.020	7.9788	1.472×10^{-2}	409	1.41	4.20	8.24	6.04	6.37
$100D_{n50}^2$	1.362×10^{-3}	0.010	11.2838	2.082×10^{-2}	189	1.20	3.56	8.16	5.37	5.77
A_{pile}	9.503×10^{-4}	0.00143	29.8103	5.500×10^{-2}	24	0.30	2.22	7.06	3.69	3.45

Appendix C

MATLAB Function for Calculating S/D_p, Kc_{tot}, and MOB_{tot}—Using Formulas Developed by [21,42]

```
function [S_over_Dp]=S_over_Dp(temp, rho_s, rho_w, dn50, Hs, Tp, Uc, Um, hw, Dp, ts, L, alpha_deg)
    %% Extract input parameters from the structure
    % temp = water temperature (°C);
    %rho_s = mass density armour layer (kg/m^3);
    %rho_w = water density (kg/m^3);
    %dn50 = nominal stone diameter (m);
    %Hs = significative wave height (m) measured in the tests;
    %Tp = peak period (s) measured in the tests;
    %Uc = current velocity (m/s) measured in the tests;
    %Um = orbital wave velocity (m/s) measured in the tests;
    %hw = water depth (m);
    %h_top = water depth at the top of protection (m);
    %Dp = pile diameter (m);
    %ts = armour layer thickness in units (relative to the Dn50 value)
    %L = wavelength (m) calculated using Wiberg and Sherwood (2008);
    %alpha_deg = wave–current degree angle (°);

    %% A.1: Constants
    g = 9.81; % gravity

    %% A.2: Kinematic viscosity
    nu = (1.14–0.031*(temp–15) + 0.00068*(temp–15)^2) * 1e-6;

    %% A.3: Rock properties
    d50 = dn50/0.84;
    h_top = hw–(ts * dn50);
    Delta_s = (rho_s–rho_w)/rho_w; % specific density
    d_star = d50 * (((Delta_s * g)/(nu^2))^(1/3)); %dimensionless particle diameter

    % Shields critical parameter
    theta_cr = 0.055 * (1–exp(-0.02 * d_star)) + 0.3 / (1 + 1.2 * d_star);
```

```
% Roughness height
ks = 2.5 * d50;

%% A.4: Current-related parameters
z0 = ks/30; % bed roughness lenght
CD = (0.4/(log(hw/z0)-1))^2; % drag coefficient
u_star_c = sqrt(CD) * Uc; % current-related shear velocity
tau_c = rho_w * u_star_c^2; % current-related shear stress
theta_c = tau_c/((rho_s–rho_w) * g * d50); % current-related Shields parameter
MOBc = theta_c/theta_cr; % current-related relative mobility
KCc = (Uc * Tp)/Dp; % current-related KC number

%% A.5.1: Correction factor K_top for velocity at top of scour
K_top = sinh((2 * pi * hw)/L)/sinh((2 * pi * h_top)/L); % correction factor for orbital velocity on top of scour protection
uw_top = K_top * Um; % wave velocity at top
Aw_top = (uw_top * Tp)/(2 * pi); % wave orbital motion amplitude on top of scour protection

%% A.5.2: Wave friction factor
A_ks = Aw_top/ks;
if A_ks > 0.2 && A_ks < 2.92
fw = 0.32 * A_ks^(−0.8);
elseif A_ks >= 2.92 && A_ks < 727
fw = 0.237 * A_ks^(−0.52);
elseif A_ks >= 727
fw = 0.04 * A_ks^(−0.25);
else
error('Awa/ks value must be greater than 0.2 for valid friction factor calculation.');
end

%% Wave shear velocity and stress
u_star_w = (sqrt(0.5 * fw)) * uw_top; % wave-related shear velocity
tau_w = rho_w * u_star_w^2; % wave-related bed shear stress
theta_w = tau_w/((rho_s–rho_w) * g * d50); % wave-related shields parameter
MOBw = theta_w/theta_cr; % wave-related relative mobility
KCw = (uw_top * Tp)/Dp; % wave-related KC number

%% A.6: Combined shear stress and mobility
tau_m = tau_c + 1.2 * tau_c * ((tau_w/(tau_c + tau_w))^3.2); % Mean combined current- and wave-related bed shear stress
alpha_rad = deg2rad(alpha_deg); % angle between waves and currents
tau_max = sqrt(tau_m^2 + tau_w^2 + 2 * tau_w * tau_m * cos(alpha_rad)); % max combined current- and wave-realted bed shear stress
theta = tau_max/((rho_s–rho_w) * g * d50); % combined current- and wave-related Shields parameter
MOB = theta/theta_cr; % combined current- and wave-related relative mobility
```

```
%% Compute KC_tot (Keulegan–Carpenter number)
KC_tot = ((uw_top + Uc) * Tp)/Dp;

%% Compute S/Dp (final equation)
S_over_Dp_value = (1 + (3.93/(1 + exp(−0.74 * KC_tot + 4.75)))) * 0.07 *(MOBˆ(1.65));
% relative scour depth

%% Display results

fprintf('\n');
fprintf('KCtot: %.3f\n', KC_tot);
fprintf('KCc: %.3f\n', KCc);
fprintf('KCw: %.3f\n', KCw);
fprintf('\n');
fprintf('MOB: %.3f\n', MOB);
fprintf('MOBc: %.3f\n', MOBc);
fprintf('MOBw: %.3f\n', MOBw);
fprintf('\n');
fprintf('kinematic viscosity: %.3e\n', nu);
fprintf('delta_s: %.3f\n', Delta_s);
fprintf('D*: %.3f\n', d_star);
fprintf('\n');
fprintf('theta: %.3f\n', theta);
fprintf('theta_cr: %.3f\n', theta_cr);
fprintf('theta_c: %.3f\n', theta_c);
fprintf('theta_w: %.3f\n', theta_w);
fprintf('\n');
fprintf('tau_c: %.3f\n', tau_c);
fprintf('tau_w: %.3f\n', tau_w);
fprintf('tau_medio: %.3f\n', tau_m);
fprintf('tau_maximo: %.3f\n', tau_max);
fprintf('\n');
fprintf('ks: %.3f\n', ks);
fprintf('z0: %.3e\n', z0);
fprintf('CD: %.3f\n', CD);
fprintf('u*c: %.3f\n', u_star_c);
fprintf('u*w: %.3f\n', u_star_w);
fprintf('uw_top: %.3f\n', uw_top);
fprintf('Ktop: %.3f\n', K_top);
fprintf('Awtop: %.3f\n', Aw_top);
fprintf('A/ks: %.3f\n', A_ks);
fprintf('fw: %.3f\n', fw);
fprintf('\n');
fprintf('S/D: %.3f\n', S_over_Dp_value);

end
```

References

1. WindEurope. *Getting Fit for 55 and Set for 2050: Electrifying Europe with Wind Energy*; WindEurope: Brussels, Belgium, 2021.
2. Matutano, C.; Negro, V.; Lopez-Gutierrez, J.S.; Esteban, M.D. Scour prediction and scour protections in offshore wind farms. *Renew. Energy* **2013**, *57*, 358–365. [CrossRef]
3. Bhattacharya, S. Challenges in Design of Foundations for Offshore Wind Turbines. *Eng. Technol. Ref.* **2014**, *2014*. [CrossRef]
4. Sørensen, S.P.H.; Ibsen, L.B. Assessment of foundation design for offshore monopiles unprotected against scour. *Ocean Eng.* **2013**, *63*, 17–25. [CrossRef]
5. Saathoff, J.E.; Goldau, N.; Achmus, M.; Schendel, A.; Welzel, M.; Schlurmann, T. Influence of scour and scour protection on the stiffness of monopile foundations in sand. *Appl. Ocean Res.* **2024**, *144*, 103920. [CrossRef]
6. Fazeres-Ferradosa, T.; Taveira-Pinto, F.; Rosa-Santos, P.; Chambel, J. A review of reliability analysis of offshore scour protections. *Proc. Inst. Civ. Eng. Marit. Eng.* **2019**, *172*, 104–117. [CrossRef]
7. De Vos, L.; De Rouck, J.; Troch, P.; Frigaard, P. Empirical design of scour protections around monopile foundations. Part 2: Dynamic approach. *Coast. Eng.* **2012**, *60*, 286–298. [CrossRef]
8. Chambel, J.; Fazeres Ferradosa, T.; Miranda, F.; Bento, A.; Taveira-Pinto, F.; Lomonaco, P. A Comprehensive Review on Scour and Scour Protections for Complex Bottom-Fixed Offshore and Marine Renewable Energy Foundations. *Ocean Eng.* **2024**, *304*, 117829. [CrossRef]
9. Fazeres-Ferradosa, T.; Chambel, J.; Taveira-Pinto, F.; Rosa-Santos, P.; Taveira-Pinto, F.V.C.; Giannini, G.; Haerens, P. Scour Protections for Offshore Foundations of Marine Energy Harvesting Technologies: A Review. *J. Mar. Sci. Eng.* **2021**, *9*, 297. [CrossRef]
10. Zhang, F.; Chen, X.; Yan, J.; Gao, X. Countermeasures for local scour around offshore wind turbine monopile foundations: A review. *Appl. Ocean Res.* **2023**, *141*, 103764. [CrossRef]
11. Soulsby, R.L. *Dynamics of Marine Sands, a Manual for Practical Applications*; Thomas Telford Publications: London, UK, 1997; p. 256.
12. den Boon, J.H.; Sutherland, J.; Whitehouse, R.J.S.; Soulsby, R.L.; Stam, C.J.M.; Verhoeven, K.; Høgedal, M.; Hald, T. Scour behaviour and scour protection for monopile foundations of offshore wind turbines. In Proceedings of the European Wind Energy Conference & Exhibition, London, UK, 22–25 November 2004; p. 14.
13. Sumer, M.B.; Fredsøe, J. *Hydrodynamics Around Cylindrical Structures*; World Scientific: Singapore, 1997.
14. Whitehouse, R.J.S. *Scour at Marine Structures: A Manual for Practical Applications*; Thomas Telford: London, UK, 1998.
15. De Vos, L.; De Rouck, J.; Troch, P.; Frigaard, P. Empirical design of scour protections around monopile foundations: Part 1: Static approach. *Coast. Eng.* **2011**, *58*, 540–553. [CrossRef]
16. De Vos, L. *Optimisation of Scour Protection Design for Monopiles and Quantification of Waver Run-Up*; Faculty of Engineering, Ghent University: Ghent, Belgium, 2008; p. 278.
17. Van der Meer, J.W. Stability of breakwater armour layers—Design formulae. *Coast. Eng.* **1987**, *11*, 219–239. [CrossRef]
18. De Schoesitter, P.; Audenaert, S.; Baelus, L.; Bolle, A.; Brown, A.; das Neves, L.; Fazeres-Ferradosa, T.; Haerens, P.; Taveira-Pinto, F.; Troch, P. Feasibility of a dynamically stable rock armour layer scour protection for offshore wind farms. In Proceedings of the ASME 2014 33rd International Conference on Ocean, Offshore and Arctic Engineering, American Society of Mechanical Engineers, San Francisco, CA, USA, 8–13 June 2014. V003T10A026.
19. Whitehouse, R.J.S.; Brown, A.; Audenaert, S.; Bolle, A.; de Schoesitter, P.; Haerens, P.; Baelus, L.; Troch, P.; Das Neves, L.; Fazeres-Ferradosa, T. Optimising scour protection stability at offshore foundations. In Proceedings of the 7th International Conference on Scour and Erosion, Perth, Australia, 2–4 December 2014.
20. Fazeres-Ferradosa, T.; Taveira-Pinto, F.; Reis, M.T.; das Neves, L. Physical modelling of dynamic scour protections: Analysis of the damage number. *Proc. Inst. Civ. Eng. Marit. Eng.* **2018**, *171*, 11–24. [CrossRef]
21. Fazeres-Ferradosa, T.; Welzel, M.; Schendel, A.; Baelus, L.; Santos, P.R.; Pinto, F.T. Extended characterization of damage in rubble mound scour protections. *Coast. Eng.* **2020**, *158*, 103671. [CrossRef]
22. Broekema, Y.B.; van Steijn, P.W.; Wu, M.; Robijns, T. Predicting loose rock scour protection deformation around monopiles using the relative mobility number and the Keulegan–Carpenter number. *Ocean Eng.* **2024**, *300*, 117475. [CrossRef]
23. van Steijn, P.; Wu, M.; Broekema, Y. Towards a better understanding of loose rock scour protection stability around monopile foundations. In Proceedings of the 11th International Conference on Scour and Erosion (ICSE-11), Copenhagen, Denmark, 17–21 September 2023; Society for Soil Mechanics and Geotechnical Engineering (ISSMGE): London, UK, 2023.
24. Ruehl, K.M.; Forbush, D.; Lomonaco, P.; Bosma, B.; Simmons, A.; Gunawan, B.; Bacelli, G.; Michelen, C. *Experimental Testing of a Floating Oscillating Surge Wave Energy Converter*; Sandia National Laboratories: Albuquerque, NM, USA, 2019.
25. Ruehl, K.M.; Forbush, D.D.; Yu, Y.H.; Tom, N. Experimental and numerical comparisons of a dual-flap floating oscillating surge wave energy converter in regular waves. *Ocean Eng.* **2020**, *196*, 106575. [CrossRef]
26. Coe, R.G.; Bacelli, G.; Forbush, D.; Spencer, S.J.; Dullea, K.J.; Bosma, B.; Lomonaco, P. *FOSWEC Dynamics and Controls Test Report*; Sandia National Laboratories (SNL-NM): Albuquerque, NM, USA, 2020.

27. Miranda, F.; Margarida Bento, A.; Chambel, J.; Francisca-Sarmento, M.; Rosa-Santos, P.; Taveira-Pinto, F.; Fazeres-Ferradosa, T. A novel and simple passive absorption system for wave-current flumes. *Alex. Eng. J.* **2023**, *71*, 463–477. [CrossRef]
28. Chambel, J. *Analysis of Long-Term Damage of Offshore Wind Turbine Foundations*; University of Porto: Porto, Portugal, 2019.
29. Wiberg, P.L.; Sherwood, C.R. Calculating wave-generated bottom orbital velocities from surface-wave parameters. *Comput. Geosci.* **2008**, *34*, 1243–1262. [CrossRef]
30. CIRIA; CUR; CETMEF. *The Rock Manual: The Use of Rock in Hydraulic Engineering*, 2nd ed.; CIRIA: London, UK, 2007; Volume 683.
31. Chen, B.; Li, S. Experimental study of local scour around a vertical cylinder under wave-only and combined wave-current conditions in a large-scale flume. *J. Hydraul. Eng.* **2018**, *144*, 04018058. [CrossRef]
32. Sumer, B.M.; Fredsøe, J. Experimental study of 2D scour and its protection at a rubble-mound breakwater. *Coast. Eng.* **2000**, *40*, 59–87. [CrossRef]
33. Petersen, T.U.; Sumer, B.M.; Fredsøe, J.; Raaijmakers, T.C.; Schouten, J. Edge scour at scour protections around piles in the marine environment—Laboratory and field investigation. *Coast. Eng.* **2015**, *106*, 42–72. [CrossRef]
34. Schendel, A.; Welzel, M.; Schlurmann, T.; Hsu, T.-W. Scour around a monopile induced by directionally spread irregular Waves in combination with oblique currents. *Coast. Eng.* **2020**, *161*, 103751. [CrossRef]
35. Sumer, B.M.; Fredsøe, J. Scour around a pile in combined waves and currents. *J. Hydraul. Eng.* **2001**, *127*, 403–411. [CrossRef]
36. Rudolph, D.; Bos, J.K. Scour around a monopile under combined wave-current conditions and low KC-numbers. In Proceedings of the 3rd International Conference on Scour and Erosion (ICSE), Amsterdam, The Netherlands, 1–3 November 2006.
37. Sumer, B.M.; Petersen, T.U.; Locatelli, L.; Fredsøe, J.; Musumeci, R.E.; Foti, E. Backfilling of a scour hole around a pile in waves and currents. *J. Waterw. Port Coast. Ocean Eng.* **2013**, *139*, 9–23. [CrossRef]
38. Qi, W.G.; Gao, F.P. Physical modeling of local scour development around a large-diameter monopile in combined waves and current. *Coast. Eng.* **2014**, *83*, 72–81. [CrossRef]
39. Taheri, O.; Kolahdoozan, M.; Faghihirad, S. Experimental study of bed level changes in the vicinity of flap-type wave energy converters. *Ships Offshore Struct.* **2022**, *18*, 450–461. [CrossRef]
40. Chen, L.; Hashim, R.; Othman, F.; Motamedi, S. Experimental study on scour profile of pile-supported horizontal axis tidal-current turbine. *Renew. Energy* **2017**, *114*, 744–754. [CrossRef]
41. Sun, C.; Lam, W.H.; Cui, Y.; Zhang, T.; Jiang, J.; Guo, J.; Ma, Y.; Wang, S.; Tan, T.H.; Chuah, J.H. Empirical models for Darrieus-type tidal current turbine induced seabed scour. *Energy Convers. Manag.* **2018**, *171*, 478–490. [CrossRef]
42. Deltares. *Handbook of Scour and Cable Protection Methods*; Report no. Deltares250; Deltares: Delft, The Netherlands, 2024.

Disclaimer/Publisher's Note: The statements, opinions and data contained in all publications are solely those of the individual author(s) and contributor(s) and not of MDPI and/or the editor(s). MDPI and/or the editor(s) disclaim responsibility for any injury to people or property resulting from any ideas, methods, instructions or products referred to in the content.